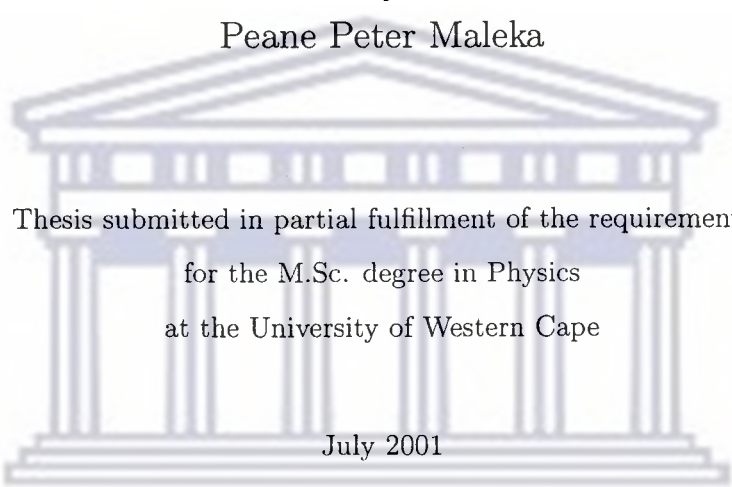


Calibration of germanium detectors for applications of
radiometric methods in South Africa.

by

Peane Peter Maleka



Thesis submitted in partial fulfillment of the requirements
for the M.Sc. degree in Physics
at the University of Western Cape

July 2001

Supervisor: Prof. R. Lindsay

Co-supervisor: Prof. Dr. R. J. de Meijer

UNIVERSITY *of the*
WESTERN CAPE

Declaration:

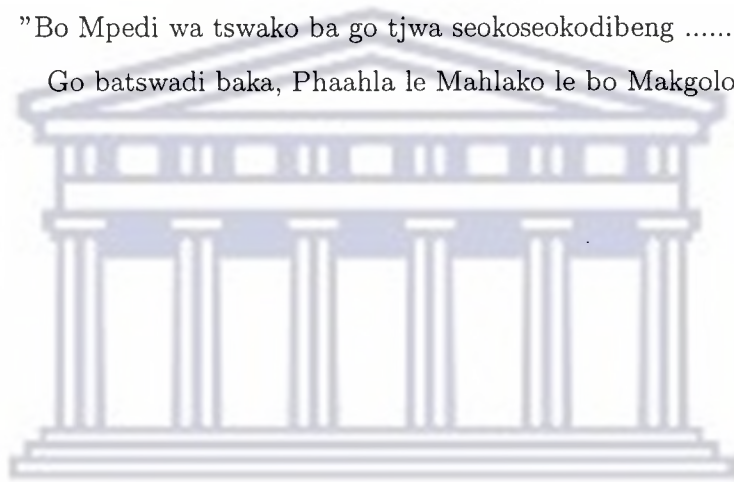
I, the undersigned, declare that the work contained in this thesis is my own original work and has not previously in its entirety or in part been submitted at any university for a degree.

Signature: *A. Aletka*.....

Date: *09/10/2001*.....

UNIVERSITY *of the*
WESTERN CAPE

”Bo Mpedi wa tswako ba go tjwa seokosekodibeng”
Go batswadi baka, Phaahla le Mahlako le bo Makgolo.



UNIVERSITY *of the*
WESTERN CAPE

ACKNOWLEDGMENTS

I am greatly indebted to the following people for the role they played in making this thesis and my academic career possible:

Prof. Robbie Lindsay, supervisor, for the help in financing and guidance in the preparations of this study,

Prof dr. Rob J. de Meijer, co-supervisor, for his indispensable guidance and suggestions in the course of this investigation,

To my parents, **Phaahla le Mahlako**, for loving, caring, understanding and giving me a chance to study and **my family** for their support and love all the way,

NGD-KVI staff, for their support during my stay in the Netherlands and special thanks to **Dr. Lars Venema** for his effort in helping me to understand the basics behind gamma-spectroscopy,

NUFFIC, for their support in financing my trip and stay at the Netherlands,

the **NAC** for allowing me the use of their equipment, funds and other resources, and special thanks to **Mr. Dawid de Villiers** and the **Physics group** for their help in discussions and computing techniques during the preparation of this manuscript,

UWC Physics department for their support and allowing me to be part of their group and **all my colleagues** for their encouragement,

my **special friend Nelisiwe**, for loving, caring and always being there for me,
to **all my friends** for their support and encouragement and

Finally to **God and my ancestors** for all the glory, power and honour, for they have carried me every step of the way!

Calibration of germanium detectors for applications of radiometric methods in South Africa.

Peane Peter Maleka

Submitted to the Department of Physics on July 2001, in partial fulfillment of the requirements for the degree of Master of Science

Abstract

All materials that are radioactive emit characteristic gamma-radiation. Natural radioactivity can be used in heavy minerals exploration and processing, as well as in understanding sediment transport processes in coastal zones [Dem97][Dem98]. Differences in radionuclide concentrations between minerals, allows the mineral species to be identified and quantified by the activity concentrations of ^{40}K , ^{232}Th and ^{238}U using a technique called radiometric fingerprinting [Dem97]. An important tool to determine sediment transport rates along the coastline is by the MEDUSA technology developed and tested at the Kernfysisch Versneller Instituut (KVI) [Dem98]. The data from the MEDUSA (Multi-Element Detector system for Underwater Sediment Activity) system needs to be calibrated first in the laboratory before field measurements can be converted to useful data. The National Accelerator Centre (NAC) is setting up a radiometric laboratory to do this by means of a high-resolution germanium detector used under low-background conditions and constant geometry.

Efficiency calibration of the detector system is the first step to achieve correct and reliable results in activity concentrations for low-level activity samples. In this study, multinuclide sources with gamma-rays in the energy of interest are used to construct energy dependent efficiency curves.

In the first method, radionuclides in the decay series of ^{232}Th and ^{238}U present in the sample material are used to construct a relative efficiency curve. This method is based on the assumption that there is uniform distribution within the sample and there is also secular equilibrium throughout the decay chains. Marinelli beakers are used as sample holders since

large volumes of samples are used to reduce measuring times. The relative detection efficiency curves are normalized with the absolute efficiency value at 1461 keV (^{40}K) from a KCl standard. The KCl standard has the same measuring volume geometry as the samples. This approach gives uncertainties smaller than 5 % and takes care of the self-attenuation by the sample material. A normalisation error can be estimated to account for the differences in sample and KCl densities and the coincident summing correction has to be applied.

The other method uses calibration standards with different densities. Self-attenuation of gamma-rays by the sample materials reduces the efficiency. Of the two standard methods (nuclide-specific and energy dependent efficiency curve) used at the KVI, the nuclide-specific method has been used in this study. In the nuclide-specific method, uncertainties in branching ratios and coincident summing no longer influence the results. The only drawback of this method is that it is only applicable for gamma-ray energies that are used in the calibration.

Results from the NAC and the KVI have been compared in an initial test to check for consistency between the laboratories. Samples were measured at the KVI and again at NAC. The results show good correlation between the two systems. Samples were also collected from a heavy mineral site to check if the locations differ in radionuclide concentration to such an extent that their radionuclide content can uniquely determine their origin. The results show that the difference in $^{238}\text{U}/^{232}\text{Th}$ ratio and ^{40}K distribution is sufficient to achieve this.



UNIVERSITY *of the*
WESTERN CAPE

CONTENTS

1	Motivation and outline of this thesis	1
1.1	Introduction	1
1.2	Why the efficiency calibration?	3
1.3	The KCl approach	4
1.4	A density dependent efficiency curve	5
1.5	Outline of the thesis	5
2	Background information on natural radioactivity and detection	7
2.1	Introduction	7
2.2	Natural radioactivity	7
2.3	Interaction of gamma-rays with matter	13
2.3.1	Photoelectric absorption	13
2.3.2	Compton scattering	14
2.3.3	Pair production	16
2.4	Detection of gamma-rays	16
2.4.1	Inorganic scintillator detectors	17
2.4.2	Semiconductor detectors	18
3	Experimental set-up and method	20
3.1	The detector and electronic set-up	20
3.2	Experimental apparatus and methodology	23
3.2.1	The HPGe γ -ray detector system set-up	23
3.2.2	The GMX γ -ray detector system set-up	23
3.2.3	Energy and FWHM calibration	24
3.2.4	Background measurement	28
3.2.5	Efficiency calibration of the detector	30

4	Results and discussion	31
4.1	Introduction	31
4.2	The density dependent efficiency relation	33
4.3	The KCl efficiency calibration approach and applications	43
4.3.1	From relative to absolute detection efficiency curve procedure	43
4.3.2	Applications	45
4.3.2.1	Sand samples from fields in Natal	45
4.3.2.2	Samples from a heavy mineral site	46
5	Conclusion	49
5.1	Conclusion and outlook	49
5.1.1	Efficiency calibration	50
	Appendices	51
	Bibliography	64



UNIVERSITY *of the*
WESTERN CAPE

LIST OF FIGURES

1-1	A method for radiometric sediment characterisation.	3
2-1	The decay chain in ^{40}K series	9
2-2	The decay chain in ^{232}Th series	10
2-3	The decay chain in ^{238}U series	11
2-4	The relative importance of the 3 major types of γ -ray interactions	14
2-5	Compton scattering process	15
3-1	Block diagram of the electronic set-up for γ -ray spectrometry	21
3-2	Block diagram of the detector beaker geometry set-up	24
3-3	FWHM calibration plot	27
4-1	Efficiency energy curves for the standards with $\rho=663.5$ and 989.9 kg m^{-3}	36
4-2	Efficiency energy curves for the standards with $\rho=1220.3$ and 1592.3 kg m^{-3}	37
4-3	By including the branching ratios for figures in Fig 4-1 to 4-2	38
4-4	Nuclide-specific efficiency <i>vs.</i> density for given γ -ray energies	39
4-5	From relative to absolute efficiency curve as function of γ -ray energy	45
4-6	Activity concentrations of the ^{40}K from the different sampling locations	47
4-7	Activity concentrations of ^{238}U , ^{232}Th as function of ^{40}K activity concentration	48
A-1	Figure showing background count rate (gross) plots for all energy of interest	55
A-2	Figure showing background count rate (net) plots for all energy of interest	58
A-3	Figure showing background count rate (net) plots for all energy of interest	60
B-1	Activity concentrations of all samples from the heavy mineral site	63

LIST OF TABLES

3-1	Energy and FWHM lines used in the calibrations	26
3-2	Weighted average background count rate for the HPGe detector system	28
3-3	Weighted average background count rate for the GMX detector system	29
3-4	The continuum background count rate in the GMX detector system	30
4-1	Activity concentrations of the calibration standards	33
4-2	Radionuclide-specific efficiencies in calibration standards with different densities	35
4-3	Parameters for the linear and exponential relations fits	40
4-4	Activity concentration of the standard outside the calibration curve	41
4-5	Comparison of activity concentrations from the two laboratories	46
A-1	Uranium series background count rates (gross) in the GMX detector system	52
A-2	Thorium and ^{40}K series count rates (gross) in the GMX detector system	53
A-3	Uranium series background count rates (net) in the GMX detector system	54
A-4	Thorium and ^{40}K series count rates (net) in the GMX detector system	56
A-5	Uranium series background count rates (net) in the HPGe detector system	57
A-6	Thorium and ^{40}K series count rates (net) in the HPGe detector system	59
B-1	Sample description for the samples collected in a heavy mineral site	61
B-2	Sample description for the samples collected in a heavy mineral site	62

Chapter 1

Motivation and outline of this thesis

1.1 Introduction

Our earth is radioactive and has been ever since it was created. Radionuclides are found naturally in air, water, soil, plant and even us human-beings are radioactive. Gamma-ray spectrometry is a key technique in the study of radioactive materials. At present gamma-ray spectrometry methods (getting information about the material (radioactive) based on the γ -rays it emits) for the determination of naturally occurring radioactive materials are of great interest in Science and Technology, spanning from mineral exploration, processing, mining and sediment transport to environmental radiation monitoring [Chio00][Dem97][Tas96]. The heat produced by radioactive decay in rocks is of fundamental importance in understanding the thermal history of the Earth and interpreting the continental heat-flux data [Chio00].

Minerals in coastal sands contain natural radionuclides, and the concentrations of these radionuclides depend on the origin, mineral composition, purity and type or/and grain size distribution of the sediments. The identification of mineral species based on difference in radionuclide concentrations is termed radiometric fingerprinting [Dem97].

A sensitive method to measure natural radioactivity in the field is demonstrated by surveying areas with the **Multi-Element Detector system for Underwater Sediment Activity (MEDUSA)** [Dem97]. These field measurements have to be calibrated first in the laboratory by means of an accurate low-level activity counting system in constant geometry. A prerequisite for this

method is to be able to measure activity concentrations accurately, both in the laboratory and in the field. In Fig. 1-1, the principle procedure to characterise sediments according to their radionuclide activity concentrations is shown. This method is termed radiometric sediment characterisation. This method uses the radiometric properties of sediments, determined in the laboratory calibration and the measurements of the natural radionuclide concentrations in the field with MEDUSA. From the bottom, MEDUSA measures the gamma-ray spectra and the onboard computer combines this radiometric information with the output of other sensors in the system with the ship's navigation information given by differential(D)GPS. The data is analysed either on/off-line by first extracting the radionuclide distribution, and is then converted to sediment distribution using a radiometric fingerprint. To interpret the data collected with the MEDUSA system, the measurement made has to be converted to the activity concentrations of radionuclides present at that particular position. By collecting a number of calibration samples from the area surveyed, the activity concentrations of each sample is then measured in the laboratory settings. It is important to ensure that the sampling covers most of the area surveyed by the MEDUSA system. The data collected and analysed in the laboratory together with the MEDUSA results combined, forms one record for that particular survey. Although the set-up is meant for sea floor surveys, the MEDUSA technology can also be used in airborne or land surveys.

The main objective of this study is to explore the accuracy in the analysis of measuring activity concentrations of environmental samples (soil, water, plant, etc.) in the laboratory using the gamma-ray spectrometry method. The purpose of the system is to provide laboratory measurements to complement field measurements of activity concentration for naturally occurring nuclei (^{40}K and the γ -ray emitting nuclei in the decay series of ^{232}Th and ^{238}U) in applications such as sediment transport and mineral processing. In this study, sand will be used as test samples. To achieve this goal, two methods of efficiency calibration for the detector system are investigated:

- By first determining the relative detector efficiency curves from the uranium and thorium contents in each sample and converting the relative to absolute detection efficiency using potassium chloride (KCl) in the same measuring conditions as the samples [Cro99].

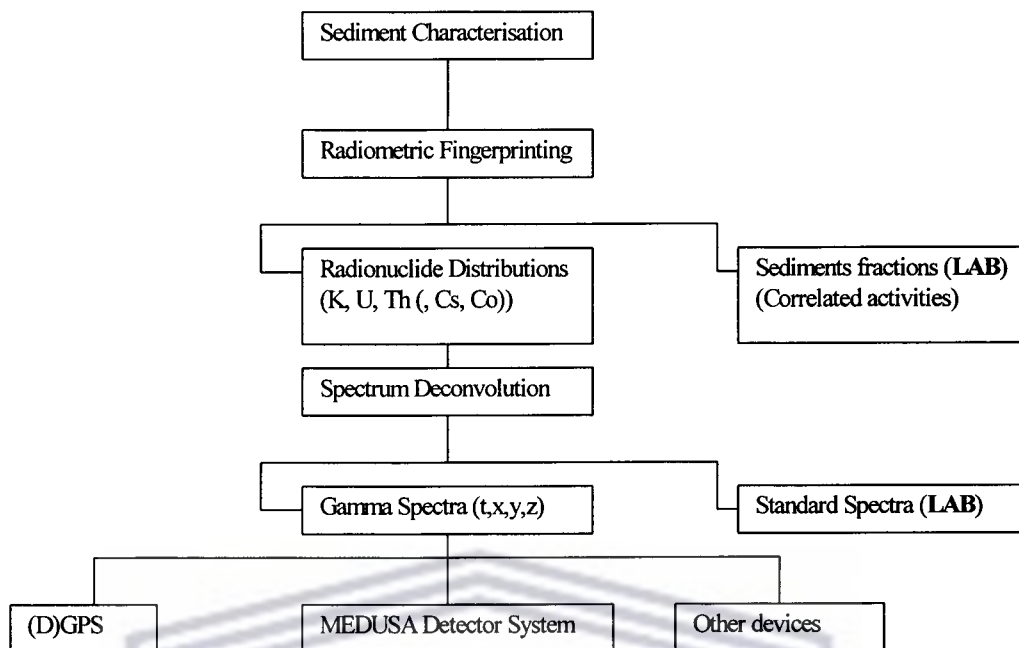


Figure 1-1: Schematic presentation of the method of radiometric sediment characterisation [Ven00]

- In the second method, the efficiency dependence on density and volume with standard sources is derived. For this calibration, nuclide-specific calibration standards are used, thus the uncertainties in branching ratios and coincidence summing are taken care of.

1.2 Why an efficiency calibration?

To achieve correct and reliable results in activity concentrations in gamma-ray spectrometry for low-level activity samples involves various steps. The first step is to calibrate the efficiency of the detector system [Tas96]. Efficiency at a certain energy is the ratio of the number of detected photons to the number of photons emitted by the source [Tro95].

For an optimal efficiency calibration of the detector, a radioactive standard source with the same radionuclides and having the same density, measuring geometry and chemical composition as the samples under study should be used [Fel92][Deb89]. Usually not all these conditions are fulfilled. Sometimes a multinuclide standard source with γ -rays in the energy range of interest

is used to compose an energy dependent efficiency curve by fitting a function through the calibration points. Then the efficiency for the gamma rays of the samples are obtained from the interpolation curve [Par95][Deb89]. Since environmental samples usually have low activity concentrations, large volumes are used to reduce measuring times. Marinelli (re-entrant) beakers are often used as sample holders in these measurements [Lav97]. The activity measurement for the Marinelli geometry is limited by two effects, namely the correction for coincident summing and self-absorption in the sample material [Dry89]. In this measuring geometry, a major portion of the sample is near the sensitive detector volume, thus optimising the efficiency and thereby minimising the systematic uncertainty due to self-absorption as compared to a cylindrical container placed on top of the detector endcap [Tro95][Deb89]. For a certain measuring geometry, the filling heights between the sample and the standard source can be carefully adjusted, but an error that will be introduced by the difference in material density between the sample and the standard source cannot be avoided [Par95][Deb89]. A minor problem is the difference in the chemical compositions since the mass attenuation coefficients of environmental materials differ slightly from calibration sources [Par95]. Depending on the measuring geometry and the desired accuracy, coincidence-summing corrections also have to be applied [Fel92]. Coincidence summing arises if radionuclide in the sample/standard emit more than one photon in sequence within the resolving time of the spectrometer and their energies deposited in the detector are added. This leads to a reduction in photopeak intensities. Especially for Marinelli beaker geometries, these corrections can be substantial (in the ^{232}Th and ^{238}U γ -ray series).

1.3 The KCl efficiency calibration approach

In this method, radionuclides in the decay series of ^{232}Th and ^{238}U present in the sample material, are used for efficiency calibration of the detector. This approach is based on the assumption that: (1) there is uniform activity distribution within the sample and (2) there is secular equilibrium throughout the decay chains so that the a number of γ -ray lines from each chain under study can be used to fit a relative efficiency curve [Cro99]. Also in this method, only samples with the same measuring geometry, volume and density as the sample used to calibrate, can be further analysed. The full-energy peak efficiency of a germanium detector can

be described in a first-order approximation for energies above 200 keV by

$$\ln \varepsilon = b - m \ln \left(\frac{E}{E_0} \right) \quad (1.1)$$

where E is the energy in keV, $E_0 = 1$ keV, while b and m are constants [Deb88]. The relative detection efficiency curves deduced using Eq. (1.1) can be normalised with the absolute efficiency value at 1461 keV of ^{40}K resulting from the KCl standard. This approximation method usually gives uncertainties smaller than 5 % of the actual value [Cro99][Fel92]. The absolute efficiency value at 1461 keV should be obtained from the KCl standard with as close as possible, the same as volume geometry and density as the samples. A small correction estimate has to be made to account for the difference in material density of the sample and the KCl. In this method, by using the uranium and thorium contents of the sample itself, self-attenuation corrections poses no problem [Fel92]. Thus the only problem is to account for radionuclides that emit gamma-rays in cascade within the resolving time of the spectrometer.

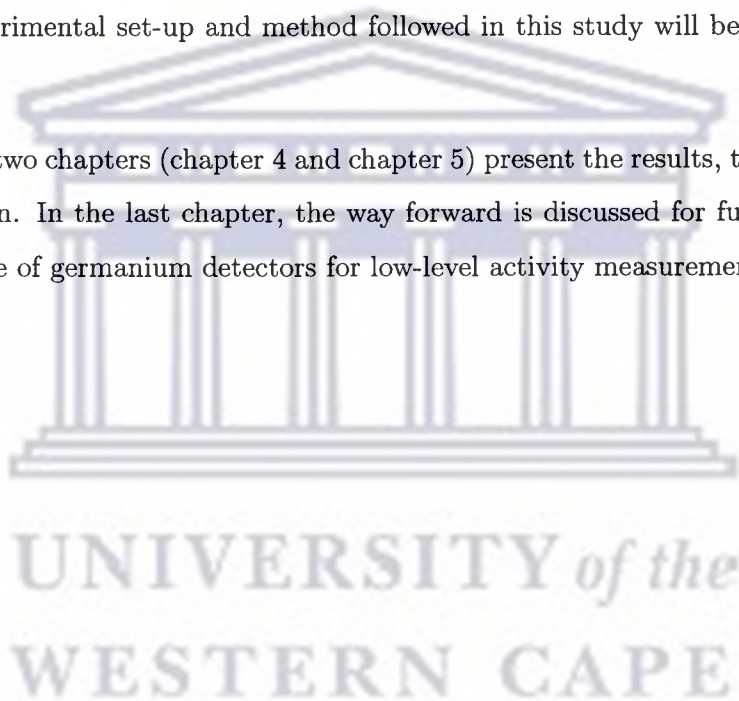
1.4 A density dependent efficiency curve

As mentioned earlier, self-attenuation corrections of gamma-rays as a results of difference in material densities of the sample materials cannot be avoided [Par95][Deb89]. Standard sources with different densities and similar filling heights were prepared to determine this relation. At the KVI in the Netherlands, two standards are used for efficiency calibration for the γ -ray detector system: (1) nuclide-specific and (2) energy dependent efficiency curve [Mal01]. In this study only the nuclide-specific calibration method will be used. The advantage of the nuclide-specific calibration is that the effects of coincident summing and uncertainties in branching ratios no longer influence the final results [Mal01]. The disadvantage of this calibration is that the method is only applicable for gamma-ray energies that are used in the calibration.

1.5 Outline of the thesis

Understanding of other methods together with the one shown in Fig. 1-1, will improve the use of naturally occurring radioactive materials. More studies are being done to utilise the gamma-rays emitted in nature to improve the knowledge for applications in Science and Technology. This study forms one part in the preparations for the applications of radiometric methods in South Africa.

- Chapter 2 will focus on studies of gamma-rays, their interactions with matter and detection. Most of the gamma-rays discussed in this study are those shown in Fig. 2-1 to Fig. 2-3.
- The experimental set-up and method followed in this study will be discussed in chapter 3.
- The last two chapters (chapter 4 and chapter 5) present the results, the discussion and the conclusion. In the last chapter, the way forward is discussed for future work pertaining to the use of germanium detectors for low-level activity measurement.



Chapter 2

Background information on natural radioactivity and γ -ray detection.

2.1 Introduction

In 1895 Roentgen began the measurement of X-rays and ever since then the studies to understand electromagnetic radiation has continued [Deb88]. Electromagnetic radiation consists of electric and magnetic waves that travel at the speed of light and include the emission of X-, γ -rays, radio waves, etc. Studies on the γ -rays started at the same time as the X-rays. An improvement in the quantitative analysis of γ - and X-rays came after the introduction of NaI(Tl) detectors in about 1948 [Deb88]. Presently, for the detection of γ -rays in the laboratory, high-resolution germanium detectors are commonly used under low-background conditions and a constant geometry.

This chapter describes the background information on the studies of γ -rays, their interactions and the detector systems used for gamma-ray spectrometry which are of interest in this study.

2.2 Natural radioactivity

In nature, most elements are stable and only few naturally occurring radionuclides with long half-life times are present. Radioactivity was the name coined by Marie Curie to describe the

phenomenon of atomic transformation, with the emission of corpuscular and or, electromagnetic radiation [Man88]. The unit of radioactivity (usually called activity) is the Becquerel (Bq) replacing the historical unit Curie (Ci) where: $1 \text{ Ci} = 3.7 \times 10^{10} \text{ Bq}$ and $1 \text{ Bq} = 1 \text{ decay per second}$. Due to radioactive decay of materials, the number of radionuclides in the material diminishes in time according to

$$N(t) = N_0 e^{-\lambda t} \quad (2.1)$$

where $N(t)$ is the number of nuclides at time t , N_0 is the number of nuclides at time t_0 , and λ is the decay constant defined as

$$\lambda = \frac{\ln 2}{T_{1/2}} \text{ where } T_{1/2} \text{ is the half-life time of the radionuclide.}$$

Radionuclides are nuclei that are unstable and disintegrate to other nuclei under the emission of radiation. Radionuclides decay mainly by the emissions of α - and β -particles or by γ -radiation, each with different properties and energies. Gamma-rays are high-energy photons with a much shorter wavelength than visible light and are produced by the transition from excited states in the nucleus. They are of interest to this study. The activity, A (in Bq) is defined as the number of nuclei that disintegrate per unit time as: $A = -\left(\frac{dN}{dt}\right)$ and hence from Eq. (2.1) as $A = \lambda N$.

For unstable nuclei, the decay product further decays until it reaches stable nuclei. Such a chain of decay products is called a decay series. In this study, it is important for the members of the decay series to be in secular equilibrium i.e. the activity concentrations are the same for all members of the decay chain. Natural radionuclides of relevance to this study are ^{40}K and the γ -ray emitting nuclei in the decay series of ^{232}Th and ^{238}U (see Fig. 2-1 to Fig. 2-3).

The half-life times of ^{238}U and ^{232}Th nuclides are longer than or comparable to the age of the Earth, indicating that the nuclei are still present in the Earth's crust. The decay chains of these three naturally occurring radionuclides are shown in Fig. 2-1 to Fig. 2-3, with the emission of β -particles indicated by diagonal lines and the emission of α -particles by vertical lines. In these decay chains, not all nuclei emit gamma-rays. The γ -ray emitters relevant to this study are, for the ^{238}U series chain: ^{214}Pb and ^{214}Bi , and for the ^{232}Th series: ^{212}Pb , ^{208}Tl and

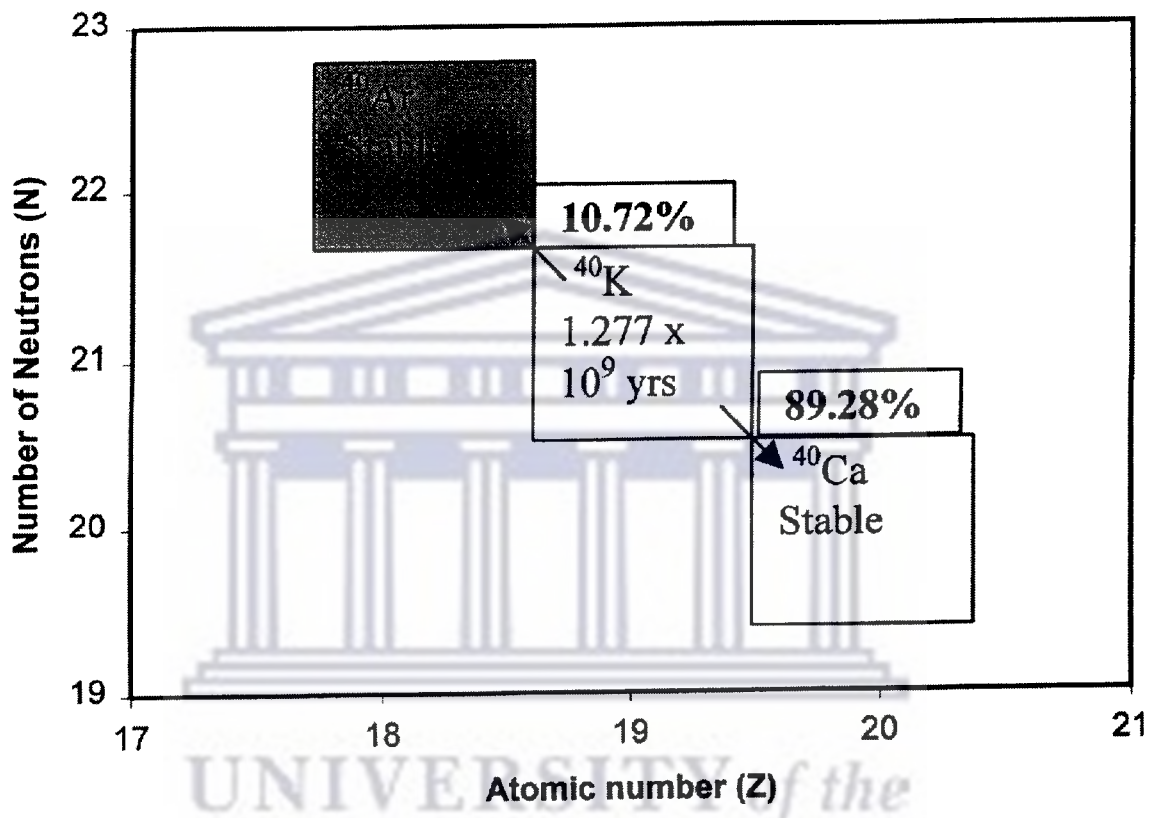


Figure 2-1: Schematic representation of the decay chain in the ^{40}K series. The grey box represents the γ -ray emitter. The diagonal lines shows a β -decay to ^{40}Ca and also the decay to the ^{40}Ar that includes an electron capture process.

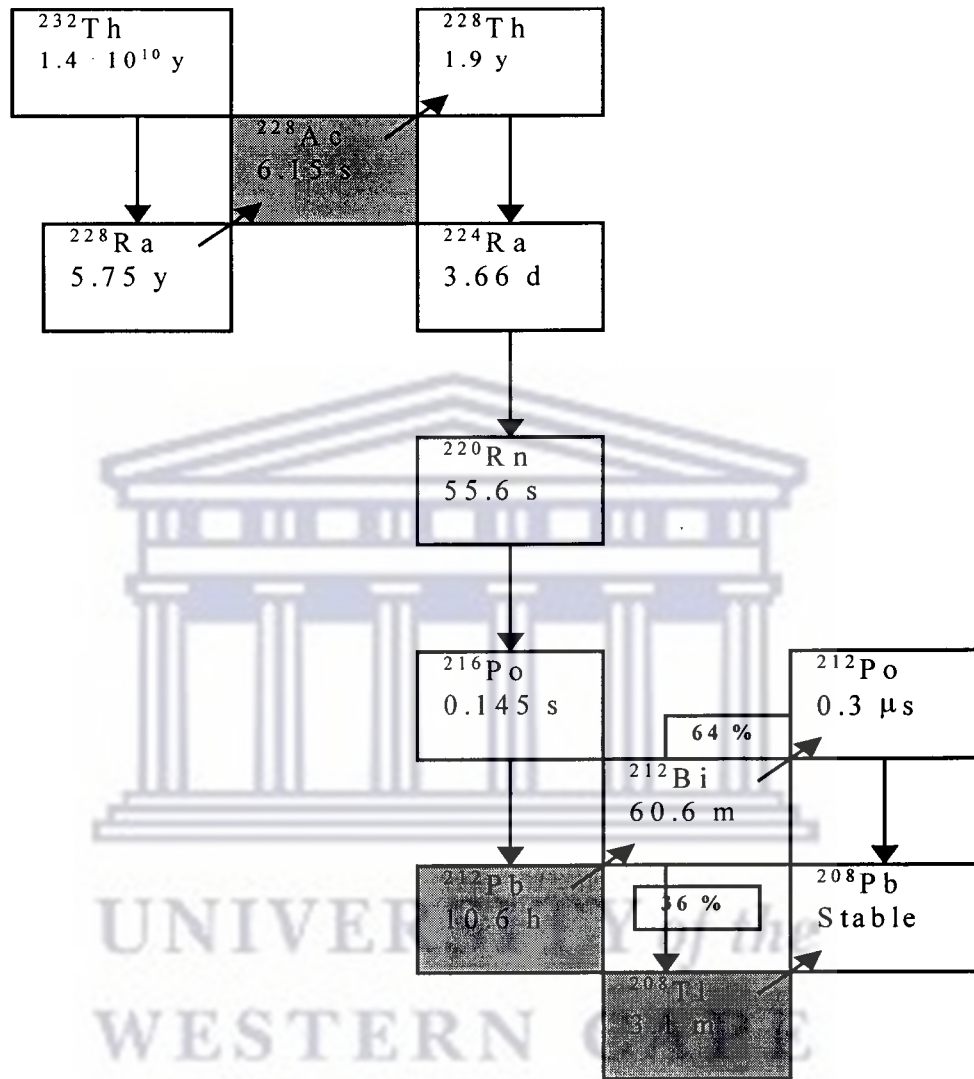


Figure 2-2: Schematic representation for the decay chain of the thorium series. The grey boxes denote γ -ray emitters relevant to this study. Vertical lines represent the α -decay and the diagonal lines β -decays. All the decays are 100 % except where indicated on the chain.

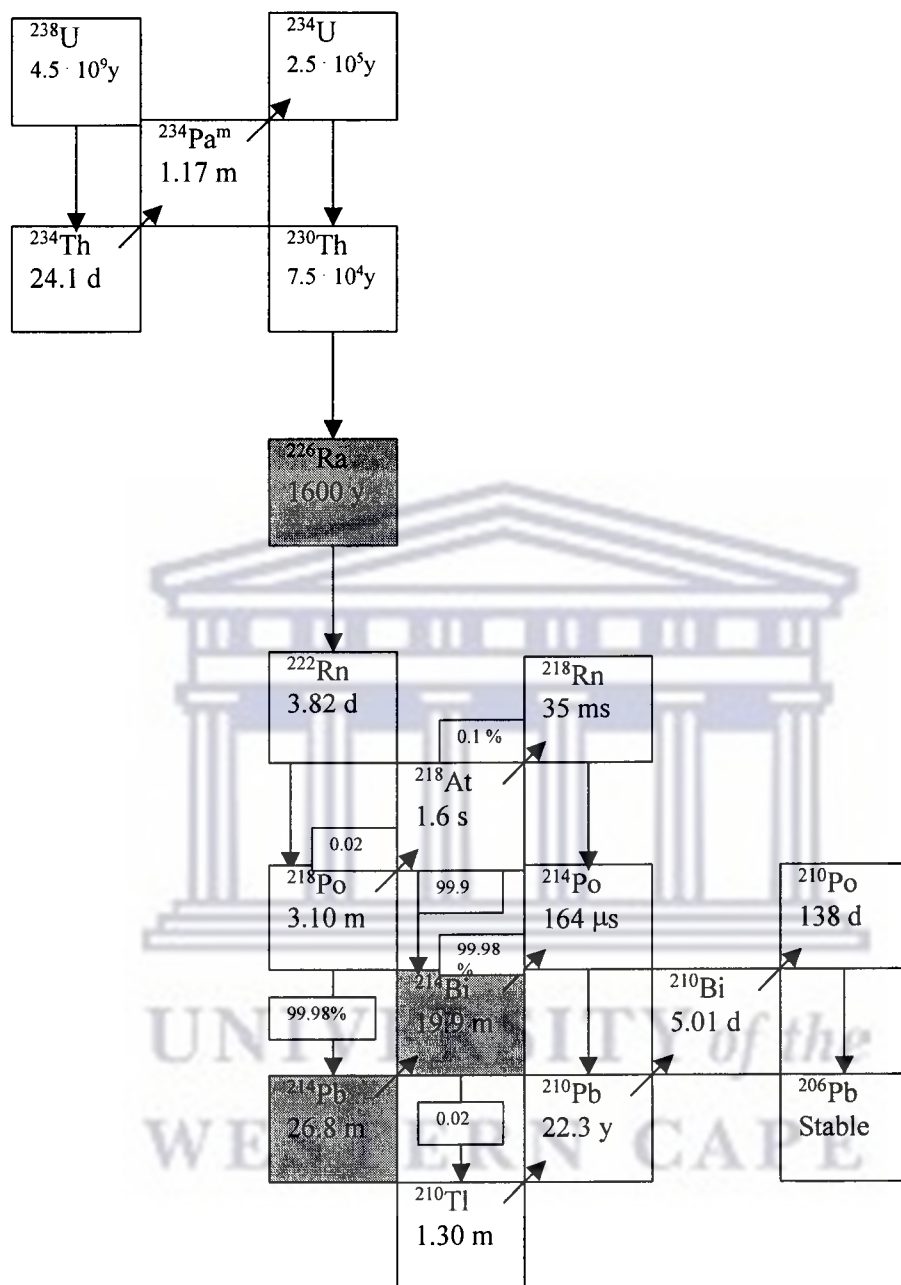


Figure 2-3: Schematic representation for the decay chain of the uranium series. The grey boxes denote γ -ray emitters relevant to this study. Vertical lines represent the α -decay and the diagonal lines β -decays. All the decays are 100 % except where indicated on the chain.

^{228}Ac , all denoted by grey boxes in Fig. 2-3 and Fig. 2-2 respectively. Also for the decay chains in figures, the decays are all 100 % except where indicated in the figures. In secular equilibrium the activity concentrations of these radionuclides should be equal to that of the parent nuclei. For the system that is not closed, there is the possibility of radon escape in the medium for the uranium series, thus the results will underestimate the ^{238}U activity concentrations. To determine this disequilibrium, concentrations of ^{238}U in a zircon sample were measured with X-ray fluorescence [Dem97], whilst the concentration of ^{214}Bi was measured with gamma-ray spectrometry, and the results within uncertainties showed no indication that the system was not closed [Dem97]. It is however known that 20-30% of radon formed in dry quartz sand does escape [Dem97]. For the ^{232}Th series, a radon isotope (^{220}Rn) is formed with its half-life time of 55 seconds. This is so short that disequilibrium poses no serious problem.

The activity concentrations of these radionuclides are calculated from the intensity of each line taking into account the mass of the sample, the branching ratio of the γ -decay, and the efficiency of the detector. The branching ratio is the statistical chance that a gamma-ray is emitted per decaying nucleus. Activity concentrations, calculated from the intensity of several γ -rays emitted by a nucleus, are grouped together to produce a weighted average activity per nuclide. The calculated activity concentration A (Bq/kg), weighted average activity concentration A_w (Bq/kg) together with its external and internal uncertainties denoted by s_{ext} and s_{int} respectively, are calculated as follows

$$A(\text{Bq/kg}) = \frac{C}{T \times m \times \varepsilon \times Br}, \quad (2.2)$$

where C (counts) is the number of counts in a photopeak, T (s) is the live time for spectrum acquisition, m (kg) the net mass of the sample, Br the branching ratio and ε the efficiency of the detector.

$$A_w(\text{Bq/kg}) = \frac{\sum \frac{A_i}{s_i^2}}{\sum \frac{1}{s_i^2}}, \quad (2.3)$$

where A_i is the activity concentration for the photopeak and s_i the uncertainty in A_i , for all $i = 1$ to N (the total number of energy lines used per series) and

$$s_{ext} = \sqrt{\frac{\sum (A_i - A_w)^2}{(N - 1)}}, \quad (2.4)$$

$$s_{int} = \sqrt{\frac{1}{\sum \frac{1}{s_i^2}}}, \quad (2.5)$$

for all $i = 1$ to N .

2.3 Interaction of gamma-rays with matter

When penetrating matter, gamma-rays interact primarily with atoms in three processes, namely photoelectric absorption, Compton scattering and pair production. These three interaction processes are relevant to the studies of gamma-rays in natural radioactivity since they span the relevant energy range, $10\text{keV} < E_\gamma < 10\text{MeV}$ (see Fig. 2-4). All these interactions involve the formation of free electrons and these electrons are slowed down in their path through the matter. These electrons create electron-ion or electron-hole pairs. These charged pairs are used in many photon detectors to detect the photon passage or its energy by measuring the quantity of charge produced.

2.3.1 Photoelectric absorption

In this process, the photon is completely absorbed by an atom and one of the atomic electrons (known as a photoelectron) is released. The kinetic energy of this electron is equal to

$$E_e = E_\gamma - E_b, \quad (2.6)$$

where E_γ is the energy of an incident photon and E_b the binding energy of the electron in its original shell. This process is dominant in the low-energy photon regions (< 0.5 MeV, see also Fig. 2-4). Photoelectric absorption increases rapidly with atomic number of the absorber atoms, and decreases rapidly with increasing photon energy. Thus the probability of interaction is expressed in cross-section (τ) per unit of mass over all ranges of photon energies (E_γ) and atomic number (Z) by

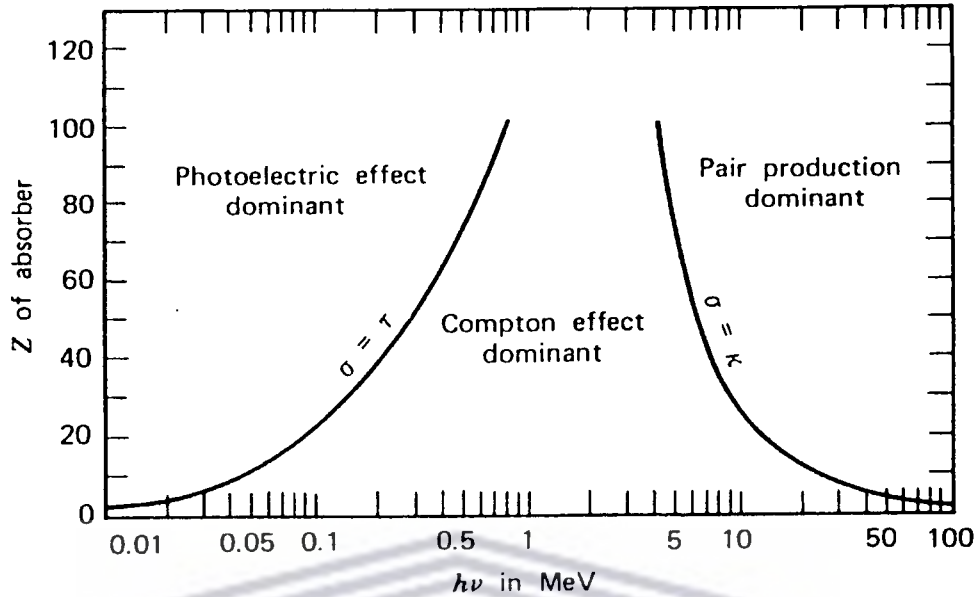


Figure 2-4: Relative importance of the three major types of gamma-ray interactions. The lines show the values of Z and E_γ ($h\nu$) for which the two neighboring effects are equal [Kno89].

$$\tau = \text{Const.} \times Z^n E_\gamma^{-3}, \quad (2.7)$$

where the exponent n varies between 3 and 5 for the gamma-ray energies of interest [Deb88].

2.3.2 Compton scattering

In Compton scattering, only a portion of photon energy is transferred to an electron, which results in a less energetic photon and a scattered electron (see Fig. 2-5). The process is dominant at higher energies of about 0.5 to 5 MeV, as shown also in Fig. 2-4. From the conservation of energy and momentum, the energies of the outgoing photon and electron is related to the angles at which they are emitted. The Compton scattering formula is given by

$$E'_\gamma = \frac{E_\gamma}{1 + (E_\gamma/m_0c^2)(1 - \cos \theta)}, \quad (2.8)$$

where E'_γ is the energy of the scattered photon, E_γ the energy of the incident photon, θ

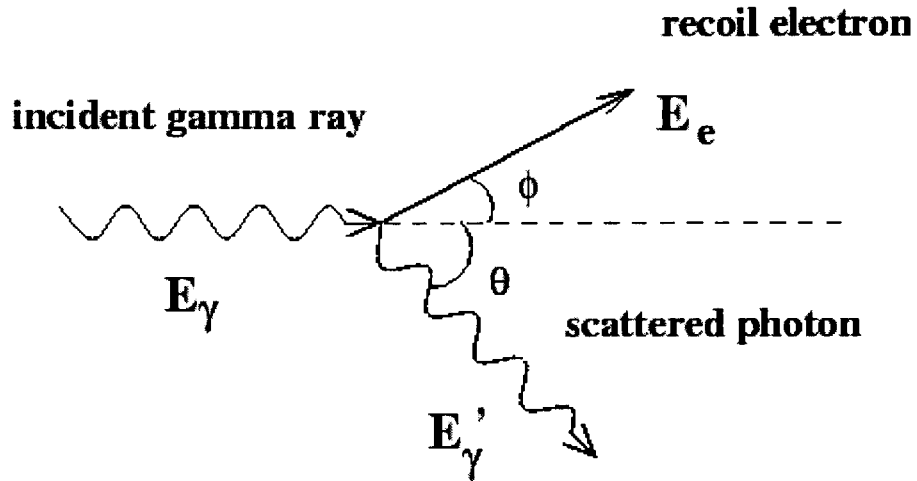


Figure 2-5: Compton scattering: A schematic representation of the interaction between a photon and an electron.

the scattering angle as in Fig. 2-5 and m_0c^2 is the rest mass of the electron (0.511MeV), and the energy of the recoil electron is given by

$$E_e = E_\gamma - E'_\gamma. \quad (2.9)$$

The probability for Compton scattering at an angle θ can be determined through quantum mechanical calculation of the process resulting in the Klein-Nishina formula for the differential cross-section per electron

$$\frac{d\sigma}{d\Omega} = Zr_0^2 \left(\frac{1}{1 + \alpha(1 - \cos\theta)} \right)^2 \left(\frac{1 + \cos^2\theta}{2} \right) \left(1 + \frac{\alpha^2(1 - \cos\theta)^2}{(1 + \cos^2\theta)[1 + \alpha(1 - \cos\theta)]} \right), \quad (2.10)$$

where $\alpha = \frac{h\nu}{m_0c^2}$ and r_0 (the classical electron radius) = 2.181 fm. The formula illustrates the strong tendency for forward scattering at high gamma-ray energies [Kra88][Kno89]. The cross-section for Compton scattering (σ) per unit mass can be approximated by

$$\sigma = \text{Const.} E_\gamma^{-1}. \quad (2.11)$$

This shows no dependence on the atomic number, hence it is independent of the medium.

2.3.3 Pair production

Pair production is due to the interaction of an incident photon in the Coulomb field of a nucleus where a positron-electron pair is created ($Q = -1.02$ MeV). The initial gamma-ray should have energy of at least twice the rest mass of an electron, thus the process requires energy in excess of 1.02 MeV. The cross-section for the process increases rapidly with atomic number and in general becomes significant for $E_\gamma > 3$ MeV. Since the maximum energy of natural gamma-rays is 2.62 MeV for this study, this process is not of great importance and will therefore not be considered in further discussion.

2.4 Detection of gamma-rays

All radiation detectors will in principle, give rise to an output pulse for each quantum of radiation that interacts within its active volume. For the detector to respond, the radiation must undergo one of the interaction mechanisms in the detector as discussed in section 2.3 above. The results of the interaction in a detector is the appearance of a given amount of electric charge within the detector active volume [Kno89]. The detector's operation involves [Deb88]:

- The conversion of the photon energy to kinetic energy of electrons,
- the production of electron-ion pairs, electron-hole pairs or excited molecular states by these electrons, and then
- the collection and measurement of the charge carriers or light emitted in the de-excitation of the molecular states.

These operations are in sequence to one another. For the conversion of photon energy to kinetic energy of electrons, detector material with high density, high atomic number and volume will give best results (see Eq. (2.7)). In this way the probability of interaction is high, hence the probability of retaining all the photon energy in the detector increases.

The ability of a detector to produce a peak from monoenergetic photons is characterised by the peak width and peak efficiency. Both peak width and efficiency are functions of the photon

energy. For the peak width (in this study the term resolution will be used), the average energy required to produce the charge-carrier pair is important, since the more pairs are created the better. Since the statistical broadening is proportional to the square of the number of pairs, the resolving power of a detector increases as the energy of the charge-pair production decreases. This resolving power is important to resolve two peaks with almost the same energy. Also the loss of charge carriers (where charges are trapped in one state) and the electronic noise will affect the width of the peak. Of all types of detectors, only two types of detector systems are of interest to this study, thus only the properties of inorganic scintillator and the semiconductor detectors will be discussed.

2.4.1 Inorganic scintillator detectors

Several crystals of alkali halides containing a small activator impurity are used as detectors. NaI(Tl) is the most generally used crystal. The thallium (Tl) is an impurity activator added to NaI to increase the probability of photon emission and to reduce self-absorption of light. Other type includes CsI(Tl), CsI(Na), $\text{Bi}_4\text{Ge}_3\text{O}_{12}$ (often called BGO), etc. Inorganic scintillation crystal operation depends on the collection of light rather than charge. In a scintillation crystal, the electrons that are generated in the processes through interaction of γ -ray photon and atoms of the crystal, will generate excited molecular states in the crystal. The photons emitted in the de-excitation of these molecular states are measured with a photo-multiplier tube (PMT). The chain of events that must take place in converting the incident photons to an electrical signal from the PMT, involves many inefficient steps. Therefore, the energy required to produce one light pulse is large (about 100 eV) and the number of generated light pulses is relatively small. The statistical fluctuation in such small number of light pulses places an inherent limitation on the resolution of a scintillation detector system. An average energy of 100 eV is needed to produce a light photon in a NaI(Tl) detector [Deb88]. This results in wider peaks for this kind of detector system. To improve the resolution, the number of light pulses (information carriers) should be increased. The biggest advantages of these detector systems are their high density and the high atomic number of iodine, hence they have a higher probability of detecting photons and a much higher chance of absorbing all of the photon energy which leads to a high efficiency. NaI(Tl) detectors are also available at affordable prices and have a wide variety of shapes and

sizes. When choosing between NaI(Tl) and the BGO, if the need for high gamma-ray counting efficiency is more important than energy resolution, the BGO is more efficient because of the higher atomic number of the bismuth and its higher density.

2.4.2 Semiconductor detectors

Semiconductor materials, mainly of silicon or germanium crystals, and they are often referred to as solid-state detectors. Amongst the types of semiconductor detectors are the lithium-drifted detectors (i.e. Ge(Li) and Si(Li)) and the high-purity germanium detectors (HPGe). For gamma-ray detection, germanium is preferred over silicon because of its higher atomic number ($Z_{Si} = 14$, $Z_{Ge} = 32$) and its smaller binding energy (E_b). The major disadvantage of the lithium-drifted detectors is that they have to be maintained at low temperatures (at 77 K) at all times because of high mobility of lithium ions in the crystal, hence the HPGe is now commonly used. For HPGe detectors cooling is also necessary and there is the possibility of using n-type semiconductor materials rather than the p-type required for the lithium-drifting process. The average energy required to produce a charge-carrier pair in semiconductor detectors is very low (for silicon = 3.81 eV and germanium = 2.96 eV) at a temperature of 77 K [Leo87].

A simplified representation of the bands in semiconductor materials include the valence band (lower) and the conduction band (upper) separated by the bandgap. In the absence of excitation, the outer electrons are bound in the valence band. The size of the band gap classifies the material as either insulator or semiconductor or conductor. For semiconductor materials the bandgap is about 1 eV. In the conduction band, the electrons are free to move under the influence of an externally applied electric field.

When a photon interacts in the crystal, bound electrons are excited from the valence band to the conduction band by the primary electron from the interaction. These secondary electrons can create additional secondary electrons if they are sufficiently energetic. Through this cascading process, the energy of the primary electron is expended in the production of many electron-hole pairs. Semiconductor materials are not free of impurities or crystal defects, they are referred to as p-type if doped with acceptor impurities or n-type for those doped with donor impurities. The effects of impurities is the introduction of holes (acceptor impurities) or the donation of electrons (donor impurities).

Comparing the NaI(Tl) and germanium detectors, if $E_{NaI(Tl)} = 100$ eV and $E_{Ge} = 3$ eV (average energies required to produce an information carrier), this implies that $\sqrt{\frac{100}{3}} \sim 6$ times better resolution for a germanium detector compared to a NaI detector. The electronic systems used, mostly in germanium detectors also introduces thermal noise, which can worsen the resolution in these detectors. The high resolution of semiconductor detectors comes with a price in that they have low atomic number compared to the inorganic scintillator detectors, thus they have lower probability of absorbing all the photon energies hence they have lower efficiencies compared to scintillator detectors. Presently semiconductor detectors of efficiencies that are comparable to the efficiency of inorganic-scintillator detectors are being manufactured (relatively expensive of course). This will improve both the quantitative and qualitative analysis for gamma-ray spectrometers.



Chapter 3

Experimental setup and method

Gamma-ray detectors work since the amount of electrical charge that is proportional to the amount of gamma-ray energy absorbed by the detector, is collected, measured and stored by the electronics system which connects to the detector system (see Fig. 3-1). In this chapter, the basic parts of the electronic systems will be discussed and also the experimental methodology for this study.

3.1 The detector and the electronic setup

In gamma-ray spectrometry, the basic parts of the experimental set-up are the detector, the electronics and the source of photons. A short overview on kinds and basic properties of detectors and source of photons have been discussed in the previous sections. A schematically depicted view of the experimental apparatus is shown in Fig. 3-1. The discussion will follow the sequence as they are shown in Fig. 3-1.

For the low-activity measurement set-up, the detector is usually protected from unwanted radiations by means of a:

- Lead castle

For measuring natural radioactivity, background suppression of the measurement is an important issue. Without reduction, the background exceeds the activity from the sources on many occasions. The source of the background spectrum is a combination of all objects around

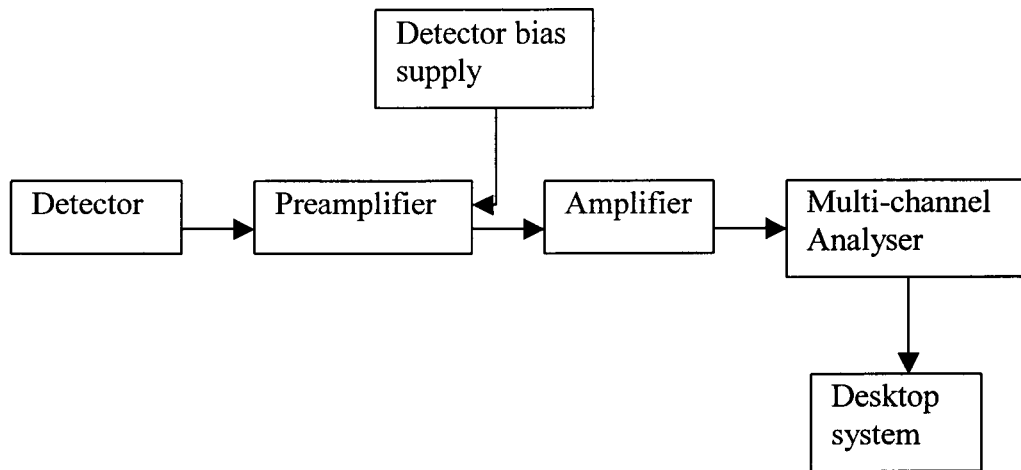


Figure 3-1: Schematic overview of a detector and its electronic setup. The detector is housed in a lead castle for low-level activity measurement to prevent unwanted radiation.

the detector that may radiate energy, as well as from cosmic rays, building materials, etc. To attenuate this unwanted radiation, the detector is shielded with the lead castle (sometimes in the form of lead bricks stacked in a way to prevent radiation from entering through the openings between the bricks). The effect of shielding is a function of energy. For germanium detectors which are more efficient at the low energy region, Compton scattering transforms high energy photons into low energy ones [Nun96]. Lead is preferred as a construction material as opposed to either iron and copper. Of the three, lead has a higher atomic number and density, thus the chances of Compton scattering decreases relative to the other two interactions [Gil95][Ver92]. For low-level measurements, a 100 mm thick lead castle is recommended with 1-2 mm of copper lining inside to absorb the lead X-rays.

- Preamplifier and the bias supply

The charge created within the detector by the interaction with the gamma-radiation is collected by the preamplifier, which converts the charge pulse to a voltage pulse and drives the pulse to the next element in the circuit. Preamplifiers in general can have various modes of operation; current-sensitive, voltage-sensitive and charge-sensitive. To minimise the signal noise (this improves the resolution), the preamplifier is usually located as close as possible to the detector. In earlier detector systems, cables were used to connect the detector to the

preamplifiers, but presently the preamplifier comes as an integral part of the detector assembly. This implies that the preamplifier is cooled down whenever the detector system is being cooled, which also reduces the electronic noise.

Almost all radiation detectors require the application of an external high voltage for their proper operation. A bias voltage provides the electric field to sweep the charge formed in the detector to be collected by the preamplifier. Depending on the detector system, all detectors have their specified high voltage value for correct operation.

- Amplifier

The voltage pulse is collected by the amplifier. The pulse shape is changed and increased in size by the amplifier. To preserve the proportionality of radiation and the pulse height, the amplifier should be linear. The pulse width is determined in the amplifier by the selection of the shaping time constant. The longer the time constant, the better the resolution for the peaks, however the longer time constant leads to random summing (the results of two or more γ -rays being detected at the same time). The other component of the amplifier, called the pole-zero cancellation differentiation, reduces the length of the undershoot and allows the system to work under moderate count rate without loss of resolution. At high count rates the variation in baseline can degrade the resolution. This problem is handled by the base-line restoration circuit of the amplifier. Also for quality results, gain stability of the amplifier is important, thus influence of temperature changes on the amplifier gain should be monitored. The pulses from the amplifier are being collected and sorted by the:

- Multi-channel analyser (MCA)

The MCA stores the sorted data, displays the data, does pre-analysis and prepares the results for output. The pulse heights are in analog form from the amplifier and they are converted to digital quantities by the ADC (analog-to-digital converter), one of the components of the MCA, and stored in the memory location as counts in channels. The MCA is housed in a computer system. The digitised form of the pulses are read and the results are further analysed on the desktop system. At this point all the information needed are displayed and ready for output.

3.2 Experimental apparatus and methodology

For this study, two detector systems were used, namely the HPGe γ -ray detector (*the detector system at NAC*) and the GMX γ -ray detector (*the detector system at KVI*) systems. The HPGe detector system was used for efficiency calibration using internal radionuclides present in the sample material, and the GMX detector system for the nuclide-specific efficiency calibration with calibration standards of different densities. These calibration methods complement each other and they are very important for both systems.

3.2.1 The HPGe γ -ray detector system set-up at the National Accelerator Centre (NAC)

The detector is a closed-end coaxial Canberra p-type detector, model GC4520 with built-in preamplifier. The detector has a crystal diameter of 62.5 mm and a length of 59.9 mm. The background radiation from unwanted materials (buildings, cosmic rays, etc.) is stopped from reaching the detector system by stacking lead bricks around the detector and two flat plates, one on top and one below. In all measurements the background spectrum was subtracted from the sample spectrum. To increase the efficiency of the system, the sample covers the detector as much as possible by using Marinelli beakers (Model 133N from Ga-ma & Associate Inc.) as sample holders. For the analysis and data acquisition in this detector system set-up, the OxfordWin-MCA programme was used.

3.2.2 The GMX γ -ray detector system set-up at the Kernfysisch Versneller Instituut (KVI)

The detector is an EG&G-Ortec n-type detector, model GMX-40195-S with built-in preamplifier. The detector has a crystal diameter of 58 mm and a length of 77.4 mm. The detector is designed for low-activity measurements with specially selected materials of low activity and a special (J-shape) cold finger to allow complete shielding. The detector is mounted in a 100 mm thick low-activity lead castle with an inner lining of 2 mm of copper to absorb low energy photons from the X-ray fluorescence of the lead. Marinelli beakers (Model 233N) were used as sample holders. In Fig. 3-2, the cross-sectional view of the detector and Marinelli beaker

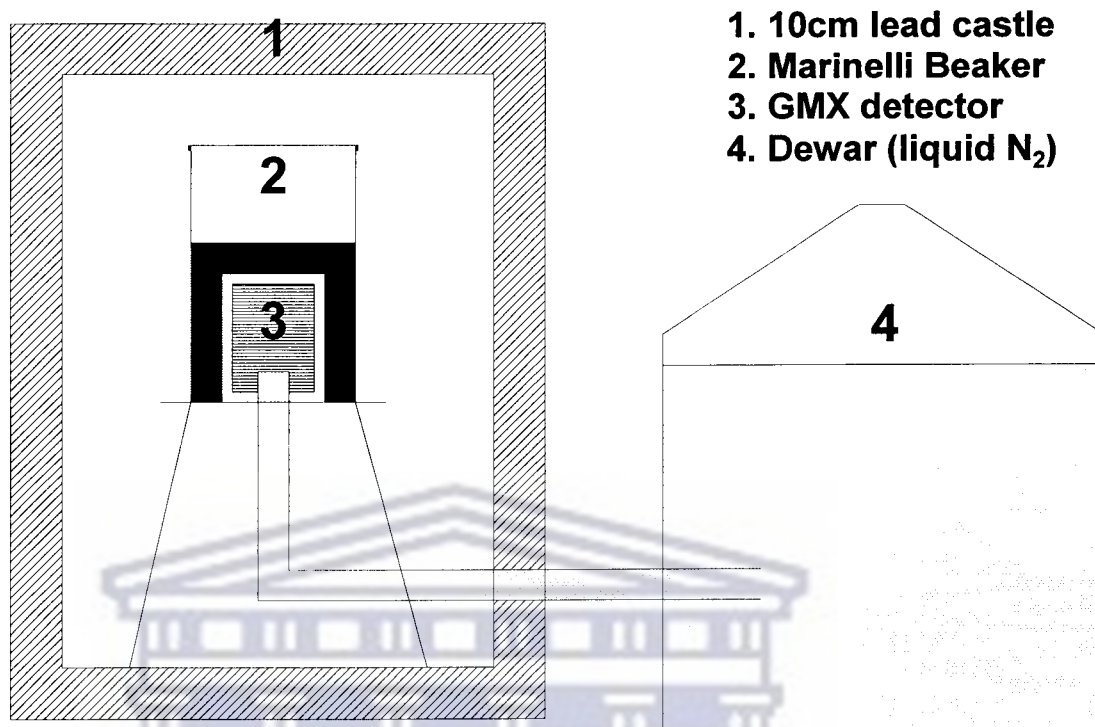


Figure 3-2: Schematic representation of the detector/beaker (Marinelli filled with analytes) set-up for the GMX detector system at the KVI. This is similar set-up to the one at NAC except that the HPGe detector is vertical upright not J-shaped.

geometry filled to 1 litre is shown. The EG&G Ortec GammaVision-32 programme was used for acquiring and analysis of spectra on the GMX detector system.

3.2.3 Energy and FWHM calibration

Before conclusions can be drawn from any measurement, the relationship between the channel number of the MCA card and the corresponding gamma-ray energy has to be established. Energy calibration is important in that in later stages of analysis, peak identification can be related to their relevant radionuclides for that specific energies. Performing an energy calibration is a straightforward procedure, however it is vital to use a calibration source with

enough energies to cover the region of interest of one's study.

A calibration standard prepared at the KVI (code 99zm502) was used for both energy and FWHM calibration of the GMX detector system. The standard was certified as by [Van00]:

KVI code	Series	Activity conc. (Bq/g)
99zm502	^{238}U	1.770 ± 0.009
	^{232}Th	0.795 ± 0.008
	^{40}K	1.99 ± 0.02

This standard has a number of intense energy lines that cover the energy range of interest for the natural radioactivity measurements. In the GammaVision-32 programme, both the energy and FWHM function are automatically fitted by

$$E = a_1 + a_2C + a_3C^2 \quad (3.1)$$

and

$$FWHM = b_1 + b_2C + b_3C^2, \quad (3.2)$$

where E is the energy (keV), C the channel number, and a_i and b_i are constant coefficients. In Table 3-1, the channel numbers, energies and the FWHM values used to fit the above functions are shown. Included also in Table 3-1 is the radionuclide name corresponding to the given energy value.

UNIVERSITY of the
WESTERN CAPE

TABLE 3-1: Energy and FWHM lines used and calculated in the calibration procedure.

Channel	Energy (keV)	Nuclide	Energy fit (keV)	FWHM (keV)	FWHM fit (keV)
253.94	46.52	²¹⁰ Pb	46.54	0.74	0.80
342.32	63.29	²³⁴ Th	62.71	0.78	0.81
704.66	129.03	²²⁸ Ac	129.03	0.88	0.87
1144.12	209.39	²²⁸ Ac	209.47	0.93	0.94
1613.36	295.09	²¹⁴ Pb	295.36	1.02	1.01
1848.89	338.42	²²⁸ Ac	338.47	1.05	1.05
1923.00	351.87	²¹⁴ Pb	352.04	1.07	1.06
2529.15	463.10	²²⁸ Ac	462.99	1.20	1.16
3185.83	583.02	²⁰⁸ Tl	583.20	1.29	1.26
3328.55	609.31	²¹⁴ Bi	609.32	1.30	1.28
4342.61	794.79	²²⁸ Ac	794.96	1.46	1.43
4977.65	911.16	²²⁸ Ac	911.21	1.56	1.53
6119.73	1120.27	²¹⁴ Bi	1120.29	1.71	1.70
7979.19	1460.83	⁴⁰ K	1460.73	2.02	1.96
8674.97	1588.23	²²⁸ Ac	1588.12	1.96	2.06
8852.22	1620.66	²¹² Bi	1620.58	2.00	2.08
9446.97	1729.58	²¹⁴ Bi	1729.47	2.14	2.16
9637.84	1764.49	²¹⁴ Bi	1764.42	2.21	2.19
12038.58	2204.09	²¹⁴ Bi	2204.03	2.47	2.50
14280.33	2614.47	²⁰⁸ Tl	2614.56	2.81	2.78

All values in Table 3-1 were fitted with the above energy and FWHM functions and the results are:

$$a_1 = 0.11 \pm 0.18, a_2 = 0.18329 \pm 0.00007 \text{ and } a_3 = (1.6 \pm 0.5) \times 10^{-8}$$

$b_1 = 0.7551 \pm 0.0012, b_2 = (8.9 \pm 0.03) \times 10^{-4}$ and $b_3 = (-4.4 \pm 1.1) \times 10^{-8}$. The regression coefficient for both of these the functions is $R^2 = 0.999$.

The energy offset is consistent with zero and the relation between the channel number and the energy is to a high degree linear with small changes at high energies (i.e. at high

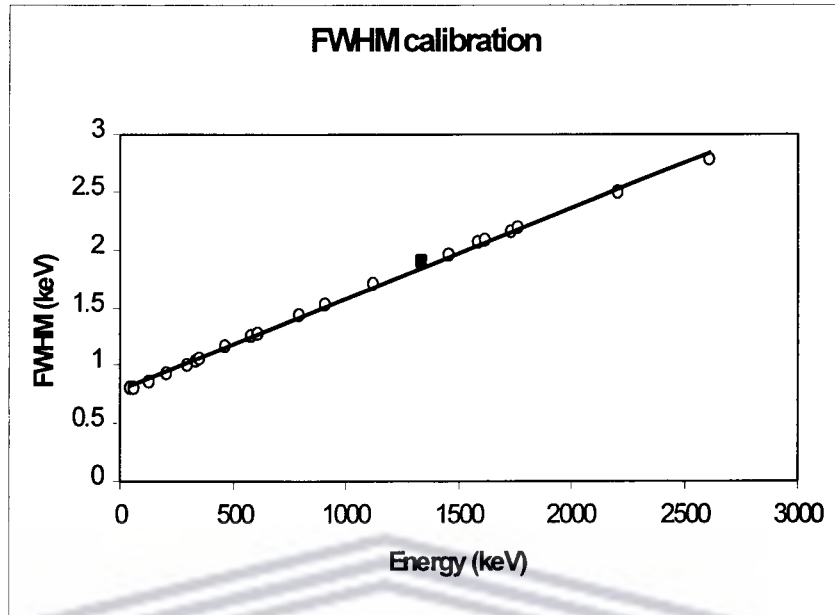


Figure 3-3: FWHM calibration plot. A data point represented by a dark square in the figure is the detector system specification value by EG&G Ortec.

channel numbers the squared term is included). Also the FWHM is linear (see Fig. 3-3), and is well described by the parameterisation, with only small differences between the fit and the experimental data as seen in Table 3-1. The regression coefficient value of 0.999 which is close to unity, verify that the fit is good. To check the detector specification of the manufacturer (Ortec) who gives a resolution of 1.9 keV for the 1333 keV (^{60}Co) line, this value is shown in Fig. 3-3. The fit results gives the resolution as better than 1.866 keV for the 1333 keV peak using the fit parameters calculated above, thus in agreement with the specifications.

An ^{152}Eu reference source, with its accurately known peaks that cover a larger number of gamma-ray energies was used to calibrate the channel numbers in terms of energies for the HPGe system. For the FWHM calibration in the HPGe detector system the ^{60}Co reference source was used and compared to the specification of the detector system by Canberra. These values are within 2 % of each other.

3.2.4 Background measurement

As mentioned earlier, background suppression is an important issue for measuring natural radioactivity, hence the background was carefully monitored for both systems.

Lead bricks of thickness of about 50 mm was stacked around the HPGe detector system. To check for consistency in the background spectra, the background measurement was done every weekend for six weekends and compared to the measurement done during the week when the laboratory is busy (i.e. the door is mostly open during the day and closed during the night). In Table 3-2, the weighted average background count rates (net) for all energies of interest in the HPGe γ -ray detector system are shown together with their uncertainties. The χ_R^2 -values are all close to unity except at the 1461 keV (^{40}K) line. The fit for this value do show that in one of the spectra, the count rates where relatively low compared to others. The reason for this is not known, but it might be related to changes that might have happened at the laboratory and were not noticed.

TABLE 3-2: Weighted average background count rates (net) for all energies of interest and their uncertainties (in/external) for the HPGe gamma-ray detector system. The corresponding reduced chi-squared values are shown.

Energy (keV)	C_w (10^{-3}cps)	σ_{int} (10^{-3}cps)	χ_R^2	σ_{ext} (10^{-3}cps)
239	6.1	0.3	1.3	0.4
295	2.6	0.3	1.3	0.3
352	5.3	0.3	1.1	0.3
583	9.2	0.2	0.9	0.2
609	11.9	0.2	1.1	0.2
911	14.9	0.2	1.7	0.3
1120	8.47	0.18	0.9	0.17
1461	130.7	0.2	2.3	0.4
1764	13.67	0.12	0.6	0.09
2615	39.95	0.12	0.4	0.08

The GMX γ -ray detector is housed in a 100 mm lead castle with the inner lining of 2 mm copper. With the generation of radon gas in the environment, the ambient radon concentration

could vary for different conditions. The background spectra for this system was monitored to check if there is any changes in the count rates relative to time. Sixteen spectra (see appendix A) were collected at different times (i.e. some during the day, night, and weekends, together with a high statistics spectrum for a continuous nine days) and analysed for further results. Table 3-3 shows the weighted average count rates (10^{-4} cps), their ex/internal uncertainties and the corresponding χ_R^2 -values. The data points represent a statistical distribution as can be seen in Table 3-3 because the χ_R^2 -values are close to unity.

A closer look of the results in Table 3-2 and Table 3-3, shows that the background count rates in the GMX detector system are about 10 times or more lower than in the HPGe detector system. This difference is likely due to the difference of the shielding of the two detector systems.

TABLE 3-3: Weighted average background count rates (net) for all energies of interest and their uncertainties (in/external) in the GMX gamma-ray detector system. The corresponding reduced chi-squared values are shown.

Energy (keV)	C_w (10^{-4} cps)	σ_{int} (10^{-4} cps)	χ_R^2	σ_{ext} (10^{-4} cps)
46.5 (^{210}Pb)	12.1	0.9	0.93	0.9
239	7.1	0.9	0.43	0.6
295	5.3	0.8	1.05	0.9
352	10.5	0.8	1.20	0.8
583	2.3	0.6	0.62	0.5
609	9.0	0.7	1.25	0.7
911	1.8	0.5	2.13	0.7
1120	2.7	0.4	0.72	0.4
1461	14.0	0.5	1.07	0.5
1764	4.2	0.4	0.66	0.3
2615	13.6	0.5	1.08	0.5

The continuum count rates were also checked to verify for all the sources that have no definite energy value. The energy region was set as shown in Table 3-4 and the content analysed and checked as in Table 3-4. At high energies (i.e. >1.2 MeV) the χ_R^2 -values are consistent with unity, yet at lower energies the χ_R^2 -values increases with the decrease in energy. The reason for

this effect is not fully understood, but is likely related to the fluctuation in the cosmic-ray flux [Dem01].

TABLE 3-4: Weighted gross average background count rates for the given energy ranges and their uncertainties (in/external) in the GMX gamma-ray detector system. The corresponding reduced chi-squared values are shown.

Range (keV)	C_w (10^{-3} cps)	σ_{int} (10^{-3} cps)	χ_R^2	σ_{ext} (10^{-3} cps)
40 - 300	463.4	0.5	5.2	1.1
300 - 600	273.4	0.4	5.0	0.9
600 - 900	139.8	0.3	2.6	0.4
900 - 1200	90.7	0.2	2.6	0.4
1200 - 1500	63.25	0.18	1.4	0.21
1500 - 1800	42.68	0.15	1.2	0.16
1800 - 2100	30.75	0.13	0.5	0.09
2100 - 2400	25.35	0.12	1.0	0.11
2400 - 2700	19.78	0.10	1.6	0.13
2700 - 3000	13.16	0.08	1.2	0.09

Based on these results and the figures shown in appendix A, one can conclude that no day-night effect in the background measurement can be detected for both systems. The steadiness of the peak intensities for the background spectra, shows that the correct background subtraction for the measurement can be used.

3.2.5 Efficiency calibration

This forms the core part of this study. Efficiency calibration of the systems plays an important role in determining accurate results in activity concentrations for low-level activity materials. Further elaboration on this topic forms a major part of the next chapter.

Chapter 4

Results and discussion

4.1 Introduction

After the energy and shape calibration and measurement of background, the efficiency is measured and calibrated for the system. To measure absolute activity concentrations, the relation between the counting efficiency and absolute activity needs to be established. The counting efficiency is dependent on geometry (solid angle of the detector as seen from the source) and possible attenuation due to absorption. For extended sources the geometry depends on the shape of the source, its mounting relative to the detector and the self-attenuation in the sample material.

In this chapter, the discussion will be divided into two parts, the first part for the GMX gamma-ray detector system and part 2 for the HPGe gamma-ray detector system.

Part I

Efficiency calibration
(Nuclide-specific) for the GMX
gamma-ray detector system at the
KVI.

UNIVERSITY *of the*
WESTERN CAPE

4.2 The density dependent efficiency relation.

Calibration standards with different densities were prepared at the KVI. The standards were sealed to avoid radon escape, thus preventing disequilibrium in the uranium concentrations. The standards were also subdivided and analysed to verify the homogeneity of these samples [Van00]. The standards were prepared in 1 litre Marinelli beaker geometry, and certified accordingly in Table 4-1. The advantage of these standards is that the effects of coincident summing and uncertainties in branching ratios no longer influence the final results, since only gamma-ray energies that are present in the standard are used. The method is therefore intrinsically more accurate.

TABLE 4-1: Activity concentration (Bq g^{-1}) in the calibration standards. Uncertainties are at 1σ level and are due to the uncertainties given in the certification sheets of the spiked samples, uncertainties in natural abundances and half lives and uncertainties from weighing procedures [Van00]. The calibration standard names are derived from the materials used and they are presented with their Dutch names, i.e. 'stearinezuur' from stearic acid; 'zetmeel' from starch; 'gips' from gypsum powder and 'kwartsmeel' from quartz powder.

Calibration standard	KVI code	Mass (g)	Radionuclide	Activity conc. (Bq g^{-1})
'stearinezuur'	99zm502	663.5	^{238}U	1.770 ± 0.009
			^{232}Th	0.795 ± 0.008
			^{40}K	1.99 ± 0.02
'gips'	99zm503	1220.3	^{238}U	0.990 ± 0.005
			^{232}Th	0.414 ± 0.004
			^{40}K	1.129 ± 0.013
'zetmeel'	99zm504	989.9	^{238}U	1.314 ± 0.006
			^{232}Th	0.511 ± 0.005
			^{40}K	1.332 ± 0.015
'kwartsmeel'	99zm505	1592.3	^{238}U	0.713 ± 0.004
			^{232}Th	0.299 ± 0.003
			^{40}K	0.774 ± 0.009

Each of the four calibration standards were measured for at least 24 hours in the GMX

system. From the recorded spectra and certified activities (in Table 4-1) of the standards, the radionuclide specific efficiencies for the relevant γ -ray energy lines were calculated according to

$$\varepsilon_E = \frac{N_E}{A_E \times m \times t} \quad (4.1)$$

where ε_E is the radionuclide-specific efficiency for the given energy line in the calibration standard, N_E (counts) the net counts in that energy line, A_E (Bq/kg) the activity concentration in the calibration standard for the given energy, m (kg) the mass of the standard and t (s) the live time for the spectrum.

The results are presented in Table 4-2. Initially these standards were measured on another system and the results were reported in Table 14 of the Van der Graaf report [Van00]. Comparison between the [Van00] results and the one in Table 4-2, shows that they agree within 10%. The difference in crystal volume of the two detector systems (the GMX and the one used by [Van00]), account for this slight difference in efficiencies. In Fig. 4-1 and Fig. 4-2, these results are verified by an energy dependent efficiency curve. In both figures, the three data points in both systems deviate from the exponential curve. The branching ratios have not been taken into account in Fig. 4-1 and Fig.4-2, since the uncertainties in coincident summing and branching ratios are deliberately ignored in this nuclide-specific efficiency method. By including the branching ratios, we get the energy efficiency curve shown in Fig. 4-3 which is similar to the usual energy dependent calibration curve of germanium detectors (see also Fig. 4-5). Also note that the 727 keV line deviates from the smooth curve because it suffers from coincident summing and it is never used in the calibration using the KCl standard. The results of the GMX γ -ray detector system shows that it is more efficient at low energies than the other system used and both systems have more or less similar efficiencies at high energies (> 1 MeV).

TABLE 4-2: Radionuclide-specific efficiencies (10^{-3} cps Bq $^{-1}$) for the relevant gamma energies of the four calibration standards with density ρ (kg m $^{-3}$)

Series	Radio nuclide	γ -energy (keV)	Efficiencies for different densities.			
			'stearinezuur'	'zetmeel'	'gips'	'kwartsmeel'
			$\rho=663.5$	$\rho=989.9$	$\rho=1220.3$	$\rho=1592.3$
^{238}U	^{214}Pb	295	6.02 ± 0.03	5.81 ± 0.03	5.75 ± 0.03	5.42 ± 0.03
		352	10.25 ± 0.05	9.96 ± 0.05	9.62 ± 0.05	9.29 ± 0.05
	^{214}Bi	609	7.72 ± 0.04	7.53 ± 0.04	7.47 ± 0.04	7.12 ± 0.04
		1120	1.625 ± 0.010	1.597 ± 0.010	1.572 ± 0.009	1.505 ± 0.009
1764		1.310 ± 0.009	1.302 ± 0.008	1.298 ± 0.008	1.264 ± 0.008	
^{232}Th	^{208}Tl	583	4.89 ± 0.05	4.80 ± 0.05	4.77 ± 0.05	4.54 ± 0.005
		2615	1.857 ± 0.02	1.825 ± 0.02	1.819 ± 0.02	1.807 ± 0.02
	^{212}Pb	239	15.20 ± 0.15	14.91 ± 0.15	14.64 ± 0.14	13.92 ± 0.14
	^{212}Bi	727	1.137 ± 0.015	1.118 ± 0.015	1.096 ± 0.015	1.06 ± 0.02
	^{228}Ac	911	3.46 ± 0.04	3.42 ± 0.04	3.40 ± 0.03	3.30 ± 0.04
^{40}K	^{40}K	1461	1.049 ± 0.012	1.06 ± 0.013	1.05 ± 0.013	1.023 ± 0.013

In Fig. 4-4, the relationship between the efficiency and the density is shown. For all these energies except the 1461 keV line, the efficiency appears to be a linear decreasing function of density. The stearinezuur standard gives for the 1461 keV line an efficiency much lower than expected given that it is less dense than other standards used. An increase in density, increases the self-absorption by the sample material, which results in a decrease in the efficiency of the detector.

To optimise the data, both the linear relation ($\epsilon = a + b\rho$) and the exponential relation ($\epsilon = a e^{b\rho}$) were fitted with a least-squares method. The results of the fit are shown in Table 4-3. For both linear and exponential relations in Table 4-3, the reduced chi-squared values look good with a few energy lines having higher or lower values than unity. The reduced chi-squared values for the linear and exponential relations are almost equal, hence the use of either relation will give almost the same results. The linear relation was used to check the discrepancy between the two efficiencies (from the actual measured values and the calculated ones using the fit parameters in Table 4-3) and the results were not more than 2 % different.

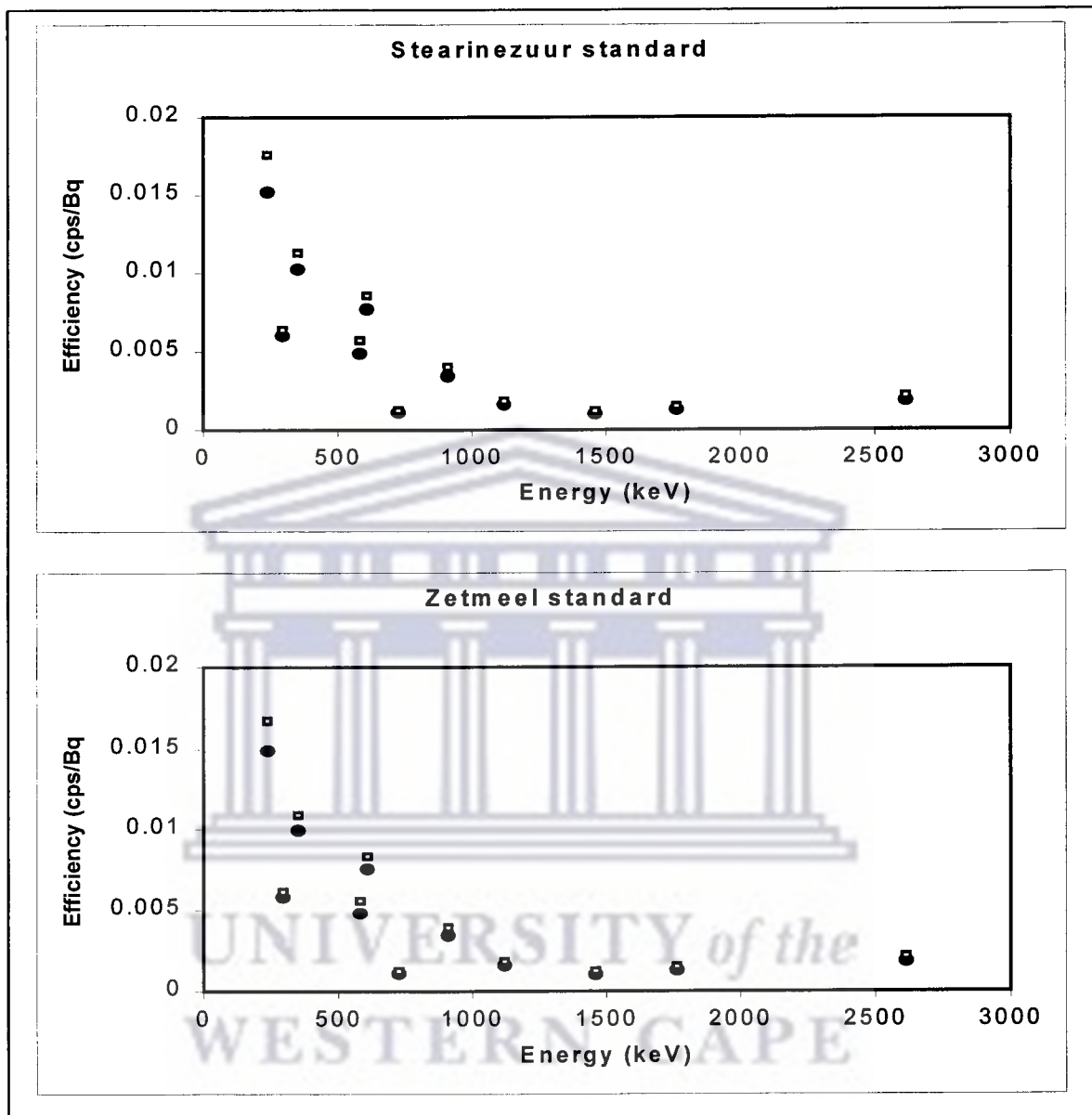


Figure 4-1: Radionuclide-specific efficiencies for the standards with $\rho = 663.5 \text{ kg.m}^{-3}$ and 989.9 kg.m^{-3} top and bottom respectively, as a function of energy for the two results. The dark spots represent the results of this study as shown in Table 4-2 and the small open squares are from [Van00] report.

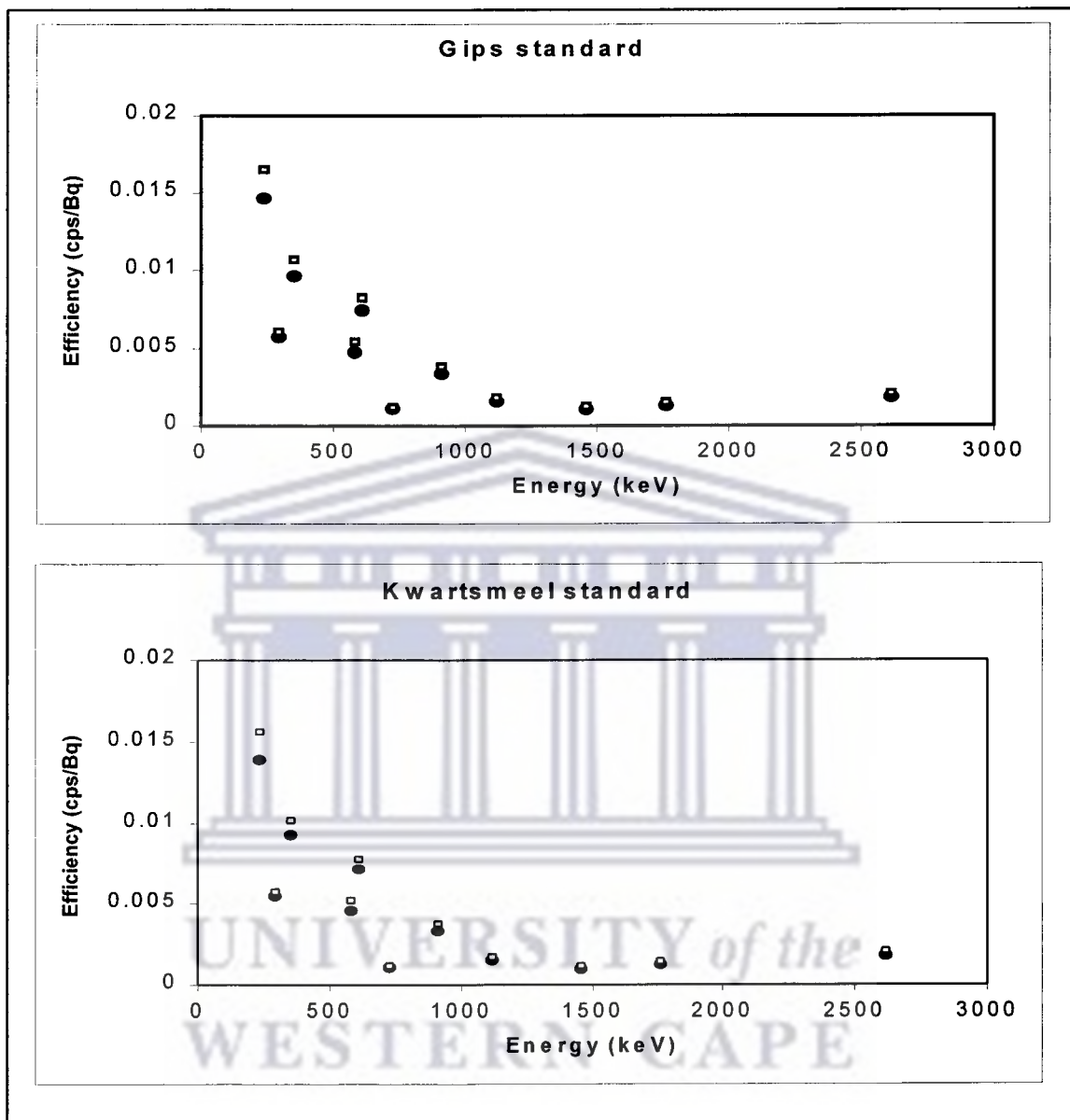


Figure 4-2: Radionuclide-specific efficiencies for the standards with $\rho = 1220.3 \text{ kg.m}^{-3}$ and 1592.3 kg.m^{-3} top and bottom respectively, as a function of energy for the two results. The dark spots represent the results of this study as shown in Table 4-2 and the small open squares are from [Van00] report.

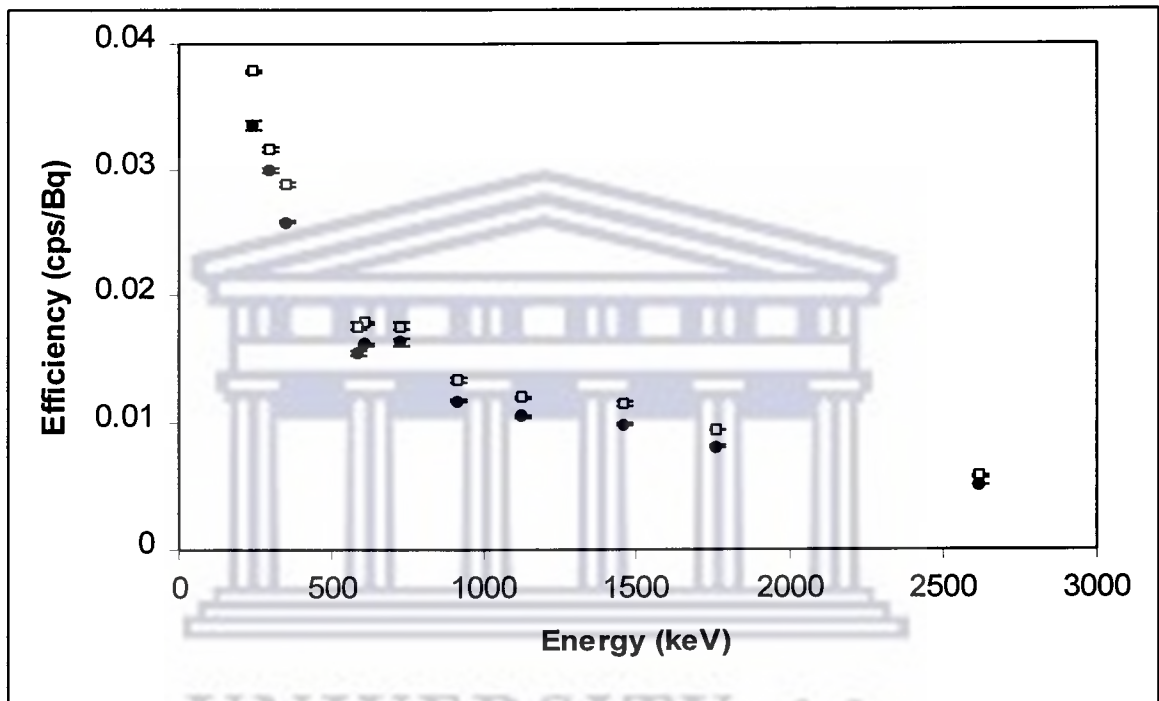


Figure 4-3: The energy efficiency curve when the branching ratios are included in figures similar to Fig. 4-1 and 4-2. The symbols have the same meanings as those in Fig. 4-1 and 4-2.

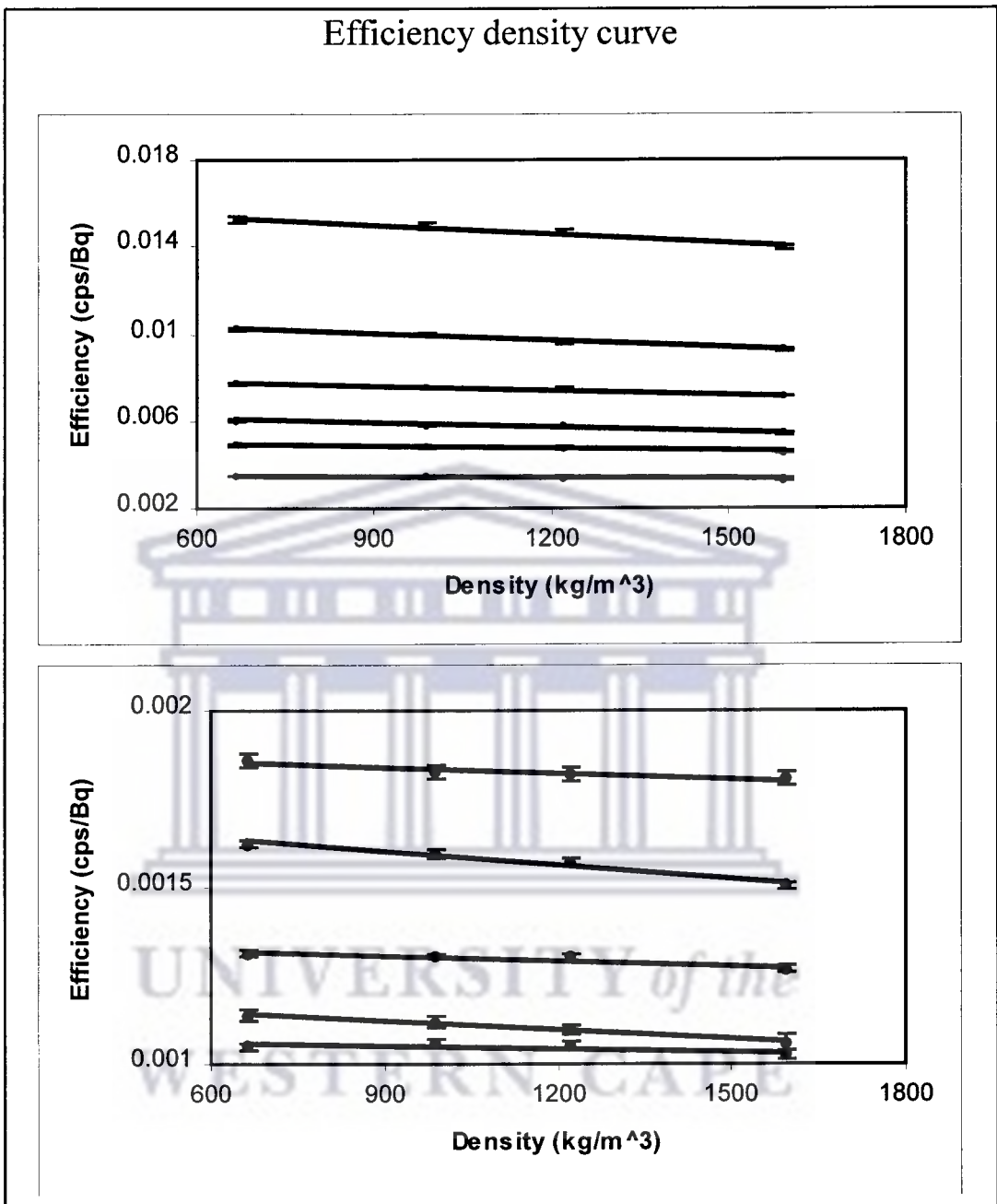


Figure 4-4: Radionuclide-specific efficiency for various γ -ray energies plotted as function of density. Error bars represent 1σ uncertainty. The plots represent energies of interest in the order from top to bottom; 239, 352, 609, 295, 583, 911, 2615, 1120, 1764, 727 and 1461 all in keV's.

TABLE 4-3: Fit parameters of both the linear and exponential relation to describe the dependence of the efficiencies on the density. Uncertainties in the brackets represent the uncertainty in the last digit.

γ energy (keV)	$\epsilon = a + b\rho$			$\epsilon = a e^{b\rho}$		
	a	b (m^3kg^{-1})	χ_R^2	a	b (m^3kg^{-1})	χ_R^2
239	$1.6221(6) \cdot 10^{-2}$	$-1.388(6) \cdot 10^{-6}$	0.82	$1.63(3) \cdot 10^{-2}$	$-9.4(1.5) \cdot 10^{-5}$	0.94
295	$6.44(6) \cdot 10^{-3}$	$-6.2(5) \cdot 10^{-7}$	3.1	$6.48(6) \cdot 10^{-3}$	$-1.08(8) \cdot 10^{-4}$	3.4
352	$1.096(9) \cdot 10^{-2}$	$-1.05(8) \cdot 10^{-6}$	1.14	$1.103(10) \cdot 10^{-2}$	$-1.08(8) \cdot 10^{-4}$	1.11
583	$5.16(9) \cdot 10^{-3}$	$-3.7(7) \cdot 10^{-7}$	1.15	$5.1782(8) \cdot 10^{-3}$	$-7.758(1.4) \cdot 10^{-5}$	1.23
609	$8.16(7) \cdot 10^{-3}$	$-6.2(6) \cdot 10^{-7}$	2.7	$8.18(4) \cdot 10^{-3}$	$-8.4(4) \cdot 10^{-5}$	2.9
727	$1.19(3) \cdot 10^{-3}$	$-8(3) \cdot 10^{-8}$	0.08	$1.20(3) \cdot 10^{-3}$	$-7(2) \cdot 10^{-5}$	0.10
911	$3.58(6) \cdot 10^{-3}$	$-1.7(5) \cdot 10^{-7}$	0.53	$3.59(6) \cdot 10^{-3}$	$-5.0(1.6) \cdot 10^{-5}$	0.55
1120	$1.72(2) \cdot 10^{-3}$	$-1.29(14) \cdot 10^{-7}$	1.63	$1.72(2) \cdot 10^{-3}$	$-8.2(9) \cdot 10^{-5}$	1.83
1461	$1.08(2) \cdot 10^{-3}$	$-2.8(1.8) \cdot 10^{-8}$	1.10	$1.07724(6) \cdot 10^{-3}$	$-2.672(5) \cdot 10^{-5}$	1.10
1764	$1.35(2) \cdot 10^{-3}$	$-4.8(1.3) \cdot 10^{-8}$	1.37	$1.35(2) \cdot 10^{-3}$	$-3.7(10) \cdot 10^{-5}$	1.40
2615	$1.89(3) \cdot 10^{-3}$	$-5(3) \cdot 10^{-8}$	0.17	$1.8860(3) \cdot 10^{-3}$	$-2.86(2) \cdot 10^{-5}$	0.17

With these results, another standard with density $\rho = 2222.1 \text{ kg m}^{-3}$ was fitted using the linear relation parameters and the results are shown in Table 4-4. The density of this calibration standard is more than the initial standards used to construct the curves in Fig. 4-4. These results are compared to the previously reported activity concentration of this sample material using two standard methods of analysis. The results of the extrapolated method compares well with earlier results except for the 1461 keV line (^{40}K) where an inconsistency was observed earlier in the efficiency density curves, see also Fig. 4-4 and Table 4-2.

In Table 4-4, the activity concentrations of the concrete standard (KVI code: 96zm149) are reported. Included also in Table 4-4, are the results from [Van00] using two different standard methods (radionuclide-specific (RNS) and the energy dependent efficiency curves (EDEC). The results of the EDEC methods are low compared to the other two sets of results where the RNS method was used. The EDEC method takes into account the effect of coincident summing and errors in branching ratio of this results, thus in these results, the coincident summing correction was applied.

With these results, the GMX detector system only needs to be efficiency calibrated for other measuring geometries to be used in future studies.

TABLE 4-4: Activity concentrations of the concrete standard with density ($\rho = 2222.1 \text{ kg m}^{-3}$) for all energy of interest and the weighted average for the given nuclides. The last two columns shows the results from the data in [Van00] report. The total uncertainties for this study (second column) comprises the counting uncertainty and the uncertainty in the efficiencies (estimated at 1 %).

Series	γ -ray Energy (keV)	RNS(GMX) Activity conc. (Bq kg ⁻¹)	RNS(Van00) Activity conc. (Bq kg ⁻¹)	EDEC(Van00) Activity conc. (Bq kg ⁻¹)
²³⁸ U	295	298 ± 3	298 ± 2	290 ± 10
	352	294 ± 3	299.6 ± 1.2	306 ± 5
	609	292 ± 3	302.8 ± 1.2	276 ± 5
	1120	308 ± 3	293 ± 3	272 ± 7
	1764	295 ± 3	295 ± 3	301 ± 7
A_w		297 ± 3	299.9 ± 1.4	290 ± 7
²³² Th	239	209 ± 2	215.2 ± 1.1	222 ± 6
	583	211 ± 2	209.1 ± 1.4	181 ± 6
	727	206 ± 2	220 ± 4	204 ± 8
	911	207 ± 2	212.7 ± 1.6	207 ± 16
	2615	210 ± 2	214.0 ± 1.9	170 ± 3
A_w		208.1 ± 0.9	213.2 ± 1.3	183 ± 10
⁴⁰ K	1461	408 ± 5	473 ± 4	501 ± 32

Part II

Efficiency calibration of the HPGe γ -ray detector system at NAC using radionuclides present in the sample materials as references.

UNIVERSITY *of the*
WESTERN CAPE

4.3 The KCl efficiency calibration approach and applications

A simple, cheap and effective method for the efficiency calibration of detectors for environmental samples is presented in this section. The relative detector efficiency curves are determined from the uranium and thorium content of each sample [Cro99] using Eq. (1.1) ($\ln \varepsilon = \ln a + b \ln(\frac{E}{E_0})$). These relative efficiency curves are scaled such that they pass through the 1461 keV line from the KCl sample. The KCl sample is used as a standard, which automatically allows for the conversion of relative efficiencies to absolute detection efficiencies. In this method, the correction for the self-absorption by the sample material is not necessary [Fel92].

4.3.1 Procedure to go from relative to absolute detection efficiency curves.

1. Assume that the two decay chains are in secular equilibrium and that the uranium content is determined by the 609 keV line of ^{214}Bi and the thorium content by the 583 keV line of ^{208}Tl . From Eq. (2.2) ($A \text{ (Bq/kg)} = \frac{C}{T \times m \times \varepsilon \times Br}$), for each energy line, $\frac{C}{Br}$ will be different for each line while the other terms will be the same for all lines in the uranium or thorium content respectively, therefore the relative efficiency was determined by dividing $(\frac{C}{Br})_E$ of each line by $(\frac{C}{Br})_{609}$ for the uranium content and $(\frac{C}{Br})_{583}$ for the thorium content such that the efficiency is unity for both the 583 keV and 609 keV lines.
2. From the uranium series results, determine the fit parameters (a and b) using Eq. (1.1) ($\ln \varepsilon = \ln a + b \ln(\frac{E}{E_0})$), with E in MeV and $E_0 = 1 \text{ MeV}$. With this a and b, determine the factor that is needed to join the thorium content to the uranium content line using $\varepsilon = aE^b$ for the efficiency of the 583 keV line and multiply all the relative efficiency values for the thorium content by this factor.
3. With the new relative efficiencies for the uranium and thorium content, again fit the equation $\ln \varepsilon = \ln a + b \ln(\frac{E}{E_0})$ and determine a and b with the new efficiency values. Calculate the relative efficiency for all the lines (both uranium and thorium) including the 1461 keV line (^{40}K) using $\varepsilon = aE^b$. At this point the relative efficiency curve is determined.
4. The absolute efficiency calibration is found by using the KCl sample. The half life of ^{40}K

is $T_{1/2} = 1.277 \times 10^9$ yrs [Bro96], the abundance = 1.17×10^{-4} of ^{40}K in potassium [Cro99] and Avogadro's number $N_A = 6.022 \times 10^{23}$ mol $^{-1}$ [Nir97]. With 1 kg of KCl (molar mass 74.551 g mol $^{-1}$ [Nir97]), the activity concentration of ^{40}K is calculated and reported as $A = 16252$ Bq kg $^{-1}$.

5. Measure the mass of KCl (dry) with the same measuring geometry as the initial samples. From the mass of KCl determine the activity (A) of ^{40}K in the KCl sample, i.e. $A(\text{Bq}) = (16252 \text{ Bq kg}^{-1} \times \text{mass of KCl in kg})$.
6. Acquire the spectrum of the KCl standard sample to determine the number of counts in the 1461 keV line. From the activity measured above in point 5, the efficiency is calculated using the equation $A (\text{Bq/kg}) = \frac{C}{T \times m \times \epsilon \times Br}$.
7. The ratio of $\epsilon(\text{point 6 above})/\epsilon(\text{point 3 above})$ gives a factor used to convert all the relative efficiencies in point 3 to an absolute efficiency curve.
8. Now the system efficiency is calibrated and the samples are ready to be analysed to determine the activity concentrations of each nuclide.
9. The ^{40}K activity concentrations may have to be corrected since the ^{228}Ac line at 1459.2 keV is very close to the 1460.8 keV line, thus the ^{40}K concentration can be overestimated for some samples. [Dem97] reported that where K and Th have the same activity concentrations, the K-line is about ten times stronger than the Th-line, and the corrections based on the strength of other Th-lines are readily made. However it becomes virtually impossible to determine the ^{40}K content for Th samples which are several orders of magnitude larger [Dem97]. In this study, the corrected activity concentration of ^{40}K is reported by subtracting 1 % of the ^{232}Th activity concentration (since the 1459.2 keV line in ^{228}Ac only contributes about 1 % of the thorium content [Bro96]).

The results of the above procedure, produced an absolute efficiency curve for the given energies (238.6, 295.2, 351.9, 583.2, 609.3, 911.2, 1120.3, 1460.8, 1764.5, 2614.5 all in keV) in Fig. 4-5.

Once the efficiency of the detector system is known, samples can be analysed and characterised according to their radionuclide content. Samples from different locations were collected

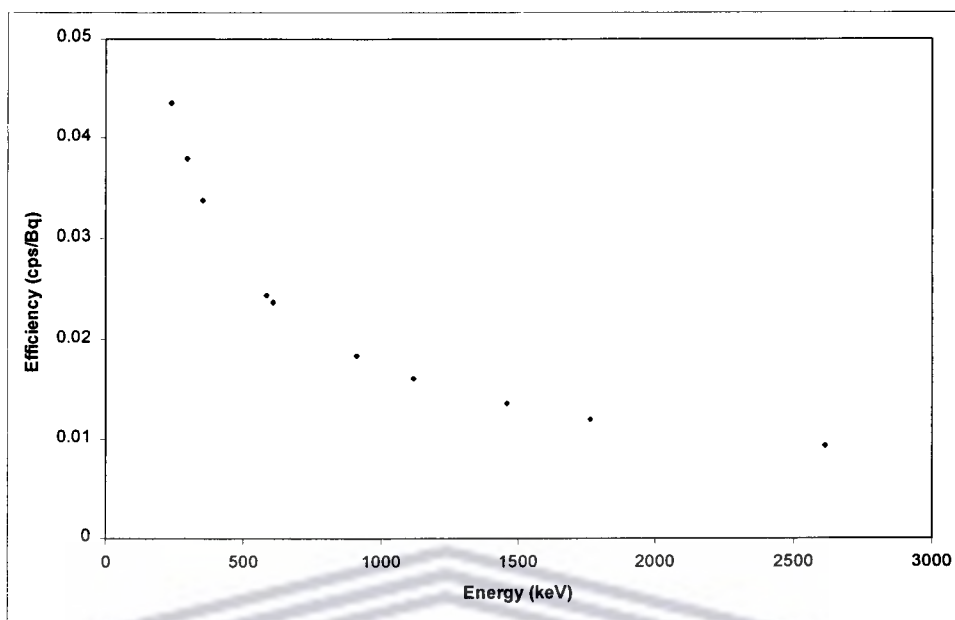


Figure 4-5: The absolute efficiency curve as a function of all energy of interest to this study. The figure is the results of the procedure followed in the above subsection.

and analysed using the relative to absolute efficiency curve procedure above.

4.3.2 Applications

In this section, samples will be analysed and categorised according to their radionuclide concentrations. Firstly the samples are analysed using two laboratories to check for consistency in both results. The purpose of these measurements is to check also how the KCl efficiency calibration approach compares with the other standard ways of efficiency calibrations. In Fig. 1-1, the laboratory part is being explored and further calibration for standard spectra will follow in the near future at NAC for the full operational of the radiometric sediment characterisation method and others of relevance to this surveying technique (MEDUSA type technology).

4.3.2.1 Sand samples from fields in Kwa-Zulu Natal.

Three samples from the sugar cane fields in Natal have been analysed with the HPGe system at NAC. These same samples were also analysed in the KVI to check on consistency in both

laboratories. Table 4-5 shows the results of the two laboratories. The overall agreement between the two results is very good. The only problem arises with the ^{40}K uncertainty especially for the Sezela sample. This is the results of the background spectrum used in lab 1 where the uncertainty in this line was found to be very low relative to the total count rates hence it underestimated the uncertainty in the final results. The energy dependent efficiency curve was used for the KVI analysis while for the NAC the relative to absolute efficiency curve method using the KCl as the standard was used. For the two calibration method results, the differences were mostly $\leq 10\%$ which is good enough for further analyses using the less expensive KCl approach.

TABLE 4-5: The activity concentrations for the comparison of two laboratories. Lab. 1 represents the NAC laboratory settings and lab. 2 the KVI one. The uncertainty in the brackets represents the uncertainty in the last digit.

Sample location	^{238}U		^{232}Th		^{40}K	
	A(Bq kg $^{-1}$)		A(Bq kg $^{-1}$)		A(Bq kg $^{-1}$)	
	lab 1	lab 2	lab 1	lab 2	lab 1	lab 2
Eston	21(1)	22.9(1.2)	41(4)	41.5(1.2)	22(4)	33(4)
Noordsburg	14.1(0.8)	13.6(0.3)	14.8(1.4)	13.7(0.4)	83(4)	74(5)
Sezela	17.6(1)	20.1(0.5)	11.9(1.2)	14.5(0.4)	885(6)	908(55)

4.3.2.2 Samples from a heavy mineral site.

Thirty seven samples were prepared in a Marinelli beaker geometry from the material types listed in Table B-1 of appendix B. The efficiency curve similar to Fig. 4-5 was determined and used for each sample under study. The aim of this analysis is to see if samples from different locations differ in radionuclide concentration to such an extent that their radionuclide activity concentration can uniquely determine their origin.

From the results (see Fig. 4-6 Fig. 4-7), one can easily see that the radionuclide distribution for the samples does determine their location. The activity concentrations of ^{40}K for all samples are shown in Fig. 4-6. The horizontal scale shows the code used for the locations of the samples (see appendix B). Based on the concentrations of ^{40}K in Fig. 4-6, the distribution of the uranium

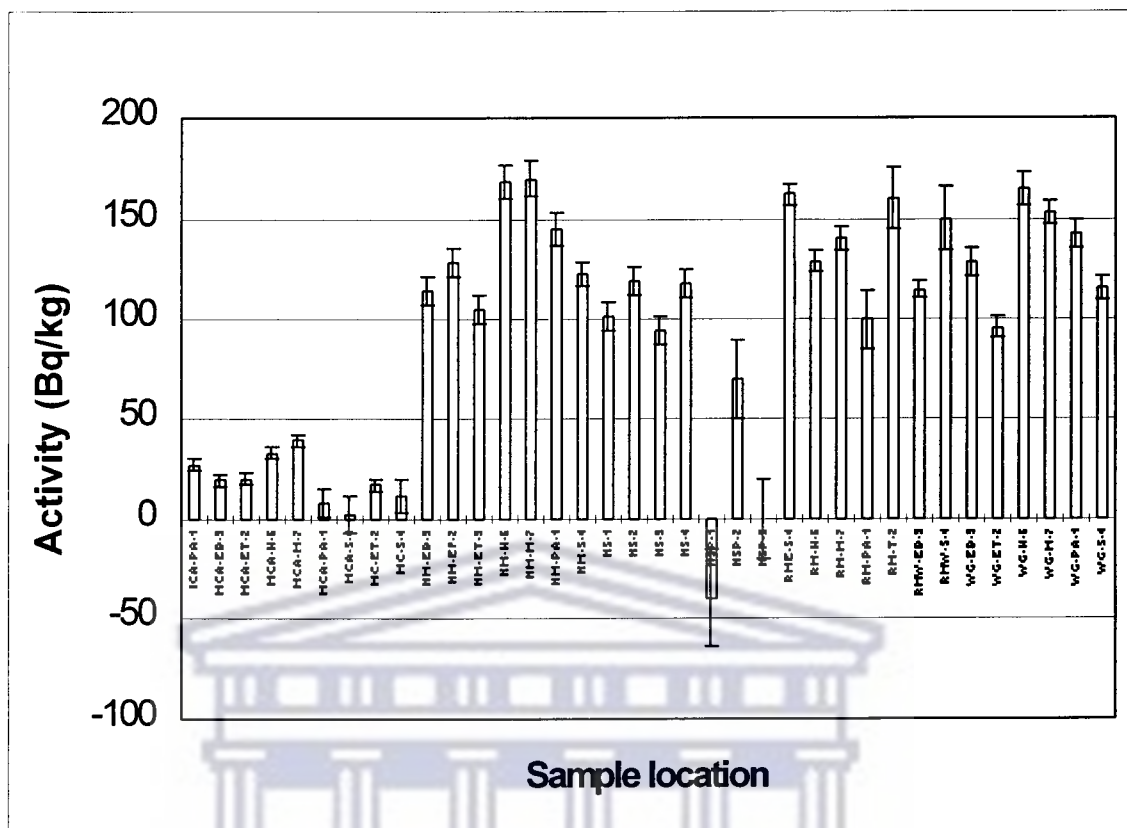


Figure 4-6: The activity concentrations of ⁴⁰K from the given sampling locations (see appendix B).

and thorium content was analysed and the ²³²Th activity concentration plotted relative to the ²³⁸U concentration in Fig. 4-7. The colours in the figures represents samples from within the same sampling area i.e. samples with the same first letter are from within the same area (see Fig. 4-6). In both figures, the symbols signify a difference in ⁴⁰K activity concentration ($\blacklozenge < 50$ Bq/kg, $50 < \blacktriangle < 153$ Bq/kg and $\blacksquare > 153$ Bq/kg).

In Fig. 4-7 it also shows that the uncertainties in the measured radionuclide concentrations are small enough so that the samples are easily separated. Their unique ²³²Th/²³⁸U ratio concentration and their ⁴⁰K activity concentration can be used to identify their origin. The application of this results will be explored in future work at NAC.

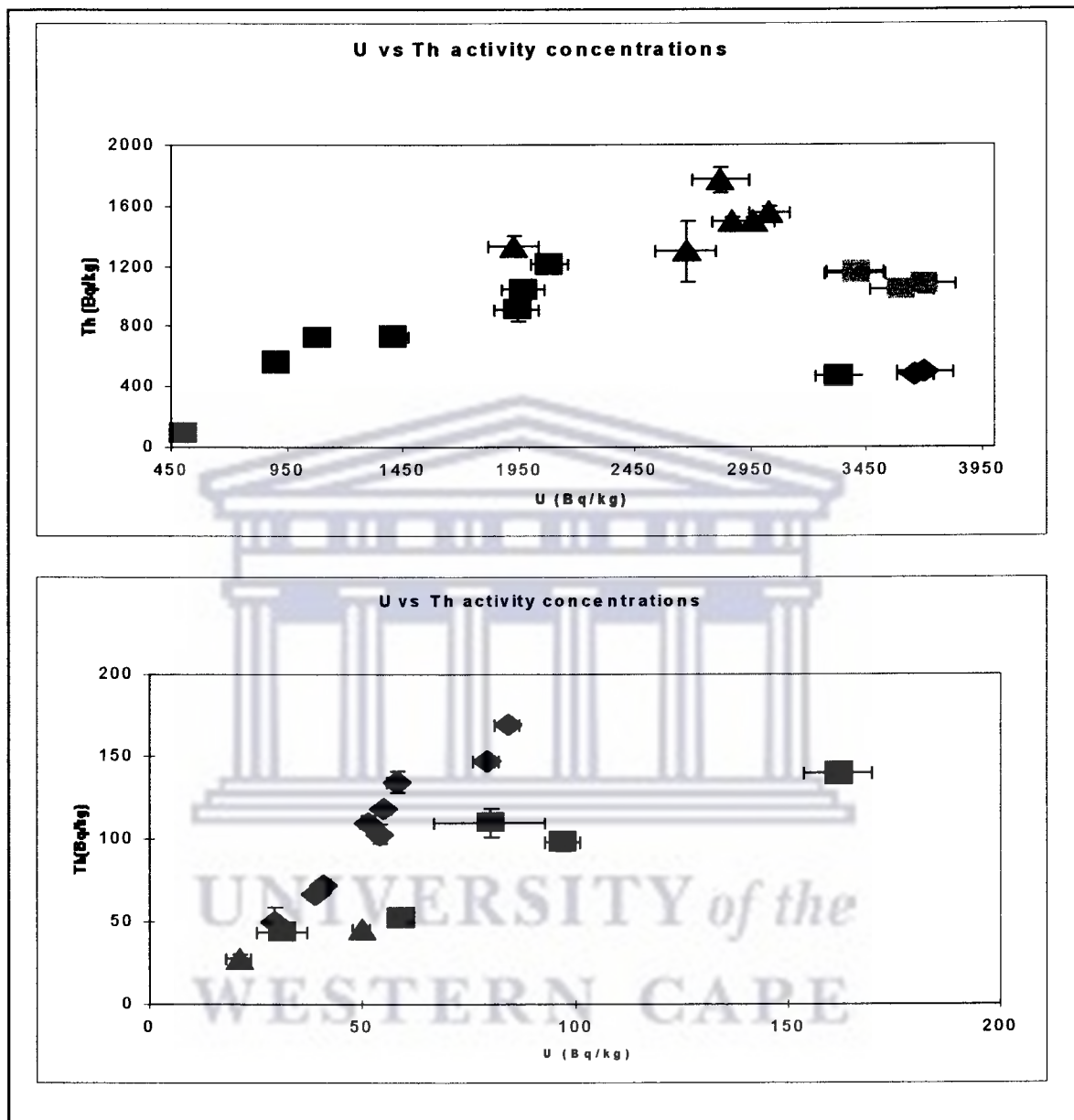


Figure 4-7: The ratio of uranium and thorium concentrations of the samples relative to the activity concentration of ^{40}K in Fig. 4-6. The symbols in the figure represent the range in activity concentrations of ^{40}K ($\blacklozenge < 50$ Bq/kg, $\blacktriangle 50 < < 153$ Bq/kg and $\blacksquare > 153$ Bq/kg) and the colours their sampling locations.

Chapter 5

Conclusion

In this chapter the results of this study is reviewed and the way forward discussed.

5.1 Conclusion and outlook

In conclusion,

- From the energy and FWHM calibration of the systems, the results seem to be consistent with the specifications. Thus a good correlation between the channel numbers of the MCA card and the energies of the nuclides are found. The fit is linear as expected with a small contribution of the squared term at high energies. FWHM calibration helps in determination of peak area and for peak fitting.
- With the background measurement results, no significant difference was observed in the peak intensities of the background over time. For the continuum analyses in the GMX detector system, there was inconsistency at low energy regions (< 1.2 MeV). This can be related to the influence of the sun on the cosmic ray background. The data does not show clear radon dependence, but the sensitivity of the system to changes in radon concentration might also be reduced because of the small nitrogen flow through the lead castle [Dem01].

Due to the steadiness of peak intensities for the background spectra, any of the background spectra can be used to correct the background influence in all other measurements (see appendix

A).

5.1.1 Efficiency calibration

The GMX gamma-ray detector system works according to specifications. The radionuclide-specific efficiency calibration is comparable to the other systems at the KVI. The first step namely for the efficiency calibration is complete. The second step will be to determine the full energy dependent efficiency curve of this system and the geometry calibration. It is presently ready for use, however it will be preferable to finish other measuring geometry calibrations first.

With the HPGe gamma-ray detector system at NAC, more calibrations are still needed. The initial results as compared to the KVI results for the Kwa-Zulu Natal samples agrees well within 10%. By including the coincident summing correction in the results together with normalisation error due to the density difference, the results should improve to within 5% thus comparable to [Cro99]. For the results in this study, no coincident summing corrections were made. For this correction, a standard source is needed to do analysis in all energies of interest and to check for any summing problem. The density difference between the sample and the KCl sample will give a constant normalisation error, hence the effect will be the same for all energy lines used. Also the efficiency as function of density for this system has to be established for further analyses of natural radioactivity samples.

Further efficiency calibration for other geometries apart from the Marinelli beaker set-up will be needed for both systems. This will help in the analyses of samples where only small quantities are available or if there is a need for checking the homogeneity of samples before transferring them to the Marinelli beaker.

Preliminary analysis of samples shows good results. The system at NAC is now available to move into second phase when the laboratory measurements are needed in the MEDUSA type survey (see Fig. 1-1) studies.

Appendix A

The background count rate check for both detector systems.

The generation of radon gas in the environment, such as from building materials and soils, causes the ambient radon concentration to vary under different conditions. This effect was investigated by measuring background count rates in different conditions. The simple procedure followed was to check the count rate change for the spectrum acquired during the day, night, weekend or for the whole week. Thus during the day, there is continuous disturbance due to the laboratory being opened and while at night it is kept closed. From the results shown below, no major effect was found to show any radon dependency (see Fig. A-1 to A-3).

The symbols in the condition column are as follows, D0, D1, etc. represent day0, day1 etc. N for night measurements, W for weekend, DN a combined day-night measurement and SUM the sum of spectra from W1(weekend1) to W2. These are the results (see Table A-1 to A-4) from the measurement using the GMX detector system.

TABLE A-1: Background gross count rate (10^{-3} cps) in the uranium series of the GMX detector.

Energy→	295	352	609	1120	1764
Conditions↓	(keV)	(keV)	(keV)	(keV)	(keV)
D0	5.56 ±0.44	5.03 ±0.42	3.02 ±0.32	1.528 ±0.230	1.319 ±0.214
N0	5.42±0.31	5.49±0.31	3.96±0.26	1.476 ±0.160	1.215 ±0.145
W1	5.86±0.16	5.41±0.15	3.71±0.13	1.454 ±0.080	1.029 ±0.067
D1	5.11±0.43	4.65±0.41	3.68±0.36	1.037 ±0.193	1.215 ±0.208
N1	5.62±0.32	5.76±0.32	3.97±0.27	1.595 ±0.170	1.106 ±0.142
D2	5.90±0.44	4.00±0.36	3.28±0.33	1.213 ±0.199	0.918 ±0.173
N2	5.71±0.31	5.23±0.30	3.26±0.24	1.545 ±0.164	1.094 ±0.138
D3	5.69±0.46	4.53±0.41	3.00±0.34	1.386 ±0.228	0.974 ±0.191
N3	5.72±0.31	5.63±0.31	3.87±0.26	1.713 ±0.171	1.387 ±0.154
D4	5.35±0.42	4.51±0.39	3.03±0.32	1.279 ±0.208	1.347 ±0.213
N4	5.64±0.31	4.85±0.28	3.61±0.25	1.488 ±0.158	1.254 ±0.145
D5	5.06±0.54	5.06±0.54	2.96±0.41	1.593 ±0.301	0.740 ±0.205
W2	5.96±0.16	5.56±0.15	3.68±0.12	1.501 ±0.080	1.112 ±0.069
DN1	5.35±0.26	4.57±0.24	3.75±0.22	1.281 ±0.127	1.040 ±0.115
DN2	5.33±0.25	5.22±0.25	3.73±0.21	1.530 ±0.134	1.039 ±0.110
SUM	5.78±0.08	5.33±0.08	3.66±0.07	1.470 ±0.042	1.102 ±0.036
w. Average	5.72±0.05	5.26±0.09	3.63±0.05	1.461 ±0.028	1.099 ±0.024
χ_R^2	0.92	2.8	1.48	0.88	0.95

TABLE A-2: Background gross count rate (10^{-3} cps) in the thorium and ^{40}K series of the GMX detector system.

Energy→	239	583	911	2615	1461
Conditions↓	(keV)	(keV)	(keV)	(keV)	(keV)
D0	6.53 ± 0.48	3.09 ± 0.33	1.597 ± 0.235	2.78 ± 0.31	2.57 ± 0.30
N0	6.48 ± 0.34	2.88 ± 0.22	1.510 ± 0.162	2.36 ± 0.20	2.85 ± 0.22
W1	6.66 ± 0.17	2.68 ± 0.11	1.633 ± 0.085	2.42 ± 0.10	2.52 ± 0.11
D1	6.90 ± 0.50	3.15 ± 0.34	1.823 ± 0.255	2.25 ± 0.28	2.93 ± 0.32
N1	7.05 ± 0.36	2.12 ± 0.20	1.577 ± 0.169	2.23 ± 0.20	2.57 ± 0.22
D2	6.88 ± 0.48	2.69 ± 0.30	1.639 ± 0.232	2.66 ± 0.30	2.29 ± 0.27
N2	6.56 ± 0.34	3.09 ± 0.23	1.510 ± 0.162	2.26 ± 0.20	2.95 ± 0.23
D3	7.15 ± 0.52	2.88 ± 0.33	1.498 ± 0.237	1.948 ± 0.270	2.77 ± 0.32
N3	6.75 ± 0.34	3.17 ± 0.23	1.764 ± 0.174	2.50 ± 0.21	2.43 ± 0.20
D4	7.02 ± 0.49	2.79 ± 0.31	1.246 ± 0.205	1.919 ± 0.254	2.66 ± 0.30
N4	6.40 ± 0.33	2.83 ± 0.22	1.689 ± 0.168	1.789 ± 0.173	2.21 ± 0.19
D5	6.43 ± 0.60	3.36 ± 0.44	1.48 ± 0.29	2.45 ± 0.37	2.73 ± 0.39
W2	6.90 ± 0.17	2.67 ± 0.11	1.678 ± 0.084	2.52 ± 0.10	2.60 ± 0.10
DN1	6.59 ± 0.29	2.32 ± 0.17	1.737 ± 0.148	2.14 ± 0.16	2.87 ± 0.19
DN2	6.96 ± 0.29	2.59 ± 0.17	1.740 ± 0.143	2.08 ± 0.16	2.58 ± 0.17
SUM	6.79 ± 0.09	2.75 ± 0.06	1.631 ± 0.044	2.33 ± 0.05	2.61 ± 0.06
w. Average	6.77 ± 0.06	2.72 ± 0.05	1.632 ± 0.029	2.32 ± 0.05	2.60 ± 0.04
χ_R^2	0.46	1.88	0.54	1.80	0.92

TABLE A-3: Background net count rate (10^{-3} cps) in the uranium series of the GMX detector system.

Energy→	295	352	609	1120	1764
Conditions↓	(keV)	(keV)	(keV)	(keV)	(keV)
D0	0.938 ± 0.625	1.875 ± 0.556	1.146 ± 0.451	0.590 ± 0.313	0 ± 0.347
N0	1.042 ± 0.451	1.163 ± 0.451	1.354 ± 0.382	0.208 ± 0.243	0.122 ± 0.243
W1	0.705 ± 0.241	1.331 ± 0.223	1.213 ± 0.188	0.346 ± 0.123	0.390 ± 0.101
D1	0.107 ± 0.643	0.250 ± 0.608	0.393 ± 0.572	0.214 ± 0.286	0.465 ± 0.286
N1	-0.218 ± 0.508	0.743 ± 0.489	0.834 ± 0.417	0 ± 0.272	0.272 ± 0.218
D2	-0.426 ± 0.688	0.557 ± 0.524	0.262 ± 0.524	0.066 ± 0.328	0.492 ± 0.229
N2	0.851 ± 0.469	1.510 ± 0.417	0.729 ± 0.365	0.608 ± 0.226	0.590 ± 0.191
D3	1.611 ± 0.637	-0.187 ± 0.637	-0.450 ± 0.562	0.075 ± 0.375	0.674 ± 0.225
N3	1.096 ± 0.462	0.651 ± 0.462	0.856 ± 0.394	0.497 ± 0.257	0.668 ± 0.223
D4	-0.067 ± 0.673	0.741 ± 0.572	0.707 ± 0.471	0.101 ± 0.337	0.236 ± 0.337
N4	0.886 ± 0.451	0.686 ± 0.418	0.217 ± 0.401	0.518 ± 0.217	0.284 ± 0.234
D5	0.057 ± 0.797	1.252 ± 0.740	0.569 ± 0.626	0.285 ± 0.455	0 ± 0.341
W2	0.283 ± 0.245	1.344 ± 0.224	0.651 ± 0.194	0.283 ± 0.123	0.444 ± 0.101
DN1	0.241 ± 0.406	1.458 ± 0.330	1.129 ± 0.317	0.013 ± 0.203	0.507 ± 0.165
DN2	0.829 ± 0.374	1.086 ± 0.362	0.864 ± 0.315	0.012 ± 0.222	0.502 ± 0.152
SUM	0.476 ± 0.128	0.925 ± 0.120	0.968 ± 0.101	0.249 ± 0.066	0.400 ± 0.057
w. Average	0.527 ± 0.085	1.049 ± 0.084	0.896 ± 0.074	0.267 ± 0.043	0.416 ± 0.036
χ_R^2	1.05	1.21	1.25	0.72	0.66

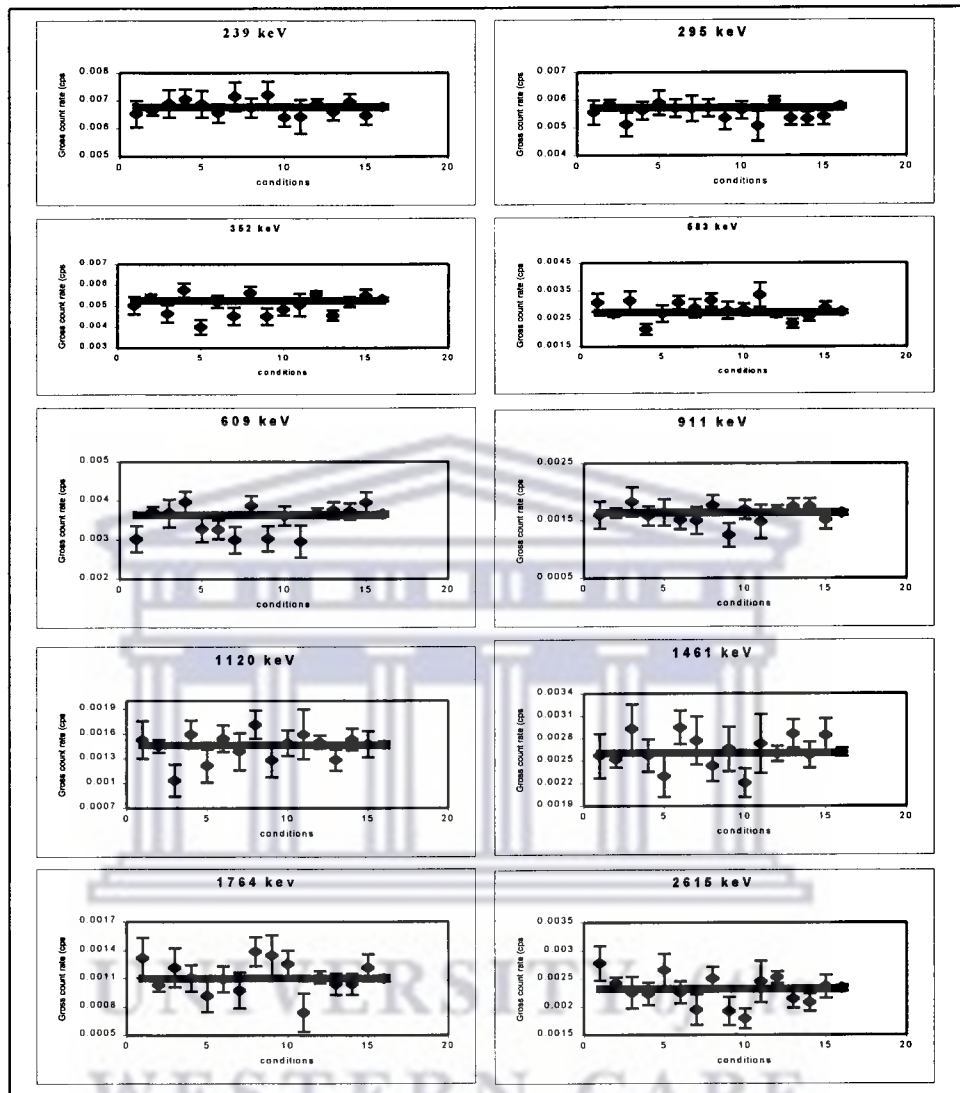


Figure A-1: This figure represents gross count rates for background spectra acquired at different conditions (see Table A-1 to A-2) in the GMX detector system. The dark horizontal solid line represents the best fit through the weighted average value for the given energy. In this plots no significant difference can be observed in each energy plot, since most points lie within the statistical uncertainties. Radon circulation in the environment can affect the uranium series count rate, yet this plot does not show any major concern.

TABLE A-4: Background net count rate (10^{-3} cps) in the thorium and ^{40}K series of the GMX detector system.

Energy→	239	583	911	2615	1461
Conditions↓	(keV)	(keV)	(keV)	(keV)	(keV)
D0	0.313 ± 0.729	0.556 ± 0.486	-0.278 ± 0.417	1.840 ± 0.417	0.972 ± 0.417
N0	0.521 ± 0.503	-0.243 ± 0.382	-0.486 ± 0.295	1.580 ± 0.260	0.920 ± 0.330
W1	0.709 ± 0.258	0.201 ± 0.175	0.171 ± 0.136	1.450 ± 0.145	1.244 ± 0.145
D1	0.393 ± 0.751	0 ± 0.536	0.179 ± 0.393	1.108 ± 0.393	1.573 ± 0.429
N1	0.834 ± 0.544	0.109 ± 0.308	0.526 ± 0.236	0.997 ± 0.308	1.251 ± 0.290
D2	0.459 ± 0.721	0.918 ± 0.426	-0.492 ± 0.426	1.180 ± 0.426	1.049 ± 0.361
N2	0.243 ± 0.521	0.434 ± 0.365	-0.087 ± 0.260	0.920 ± 0.295	1.944 ± 0.278
D3	0.712 ± 0.787	-0.262 ± 0.562	0.150 ± 0.375	1.948 ± 0.262	1.461 ± 0.412
N3	0.394 ± 0.514	-0.051 ± 0.394	0.325 ± 0.274	1.422 ± 0.291	1.576 ± 0.257
D4	1.784 ± 0.673	-0.168 ± 0.505	0.471 ± 0.269	1.313 ± 0.337	1.481 ± 0.370
N4	0.903 ± 0.485	0.452 ± 0.334	0.468 ± 0.251	1.187 ± 0.234	1.622 ± 0.217
D5	1.252 ± 0.854	0.057 ± 0.683	1.252 ± 0.285	1.650 ± 0.455	1.878 ± 0.455
W2	0.955 ± 0.258	0.402 ± 0.169	0.156 ± 0.135	1.513 ± 0.144	1.475 ± 0.140
DN1	0.418 ± 0.444	0.038 ± 0.279	0.279 ± 0.228	1.002 ± 0.241	1.750 ± 0.241
DN2	0.736 ± 0.420	0.128 ± 0.280	0.397 ± 0.210	1.285 ± 0.210	1.145 ± 0.245
SUM	0.693 ± 0.138	0.234 ± 0.094	0.086 ± 0.072	1.334 ± 0.076	1.359 ± 0.076
w. Average	0.713 ± 0.090	0.229 ± 0.061	0.178 ± 0.068	1.362 ± 0.051	1.396 ± 0.051
χ_R^2	0.43	0.62	2.1	1.08	1.07

With the HPGe detector system, spectra were acquired randomly either during the week-end, or day, night or even for the whole week. Thus the conditions are just presented as B0 (background spectrum 0) to B10.

TABLE A-5: Background net count rate (10^{-3} cps) in the uranium series of the HPGe detector system.

Energy→	295	352	609	1120	1764
Conditions↓	(keV)	(keV)	(keV)	(keV)	(keV)
B0	1.195 ±1.021	7.04 ±1.09	11.34 ±0.86	8.46 ±0.85	13.46 ±0.49
B1	1.874 ±1.074	5.68 ±1.16	10.55 ±0.64	7.94 ±0.94	13.94 ±0.56
B2	3.56 ±0.73	6.27 ±0.60	12.21 ±0.55	7.83 ±0.78	13.32 ±0.37
B3	2.22 ±0.99	3.96 ±0.91	12.23 ±0.69	7.44 ±0.71	13.23 ±0.46
B4	4.65 ±1.09	5.45 ±0.91	10.92 ±0.93	8.94 ±0.75	13.99 ±0.48
B5	3.49 ±0.93	5.01 ±1.00	13.38 ±0.87	7.47 ±0.75	13.28 ±0.46
B6	2.65 ±1.09	6.63 ±1.18	13.08 ±1.16	7.63 ±0.70	13.64 ±0.46
B7	2.03 ±0.73	4.64 ±0.80	11.96 ±0.62	8.97 ±0.43	13.62 ±0.27
B8	2.60 ±0.66	5.23 ±0.90	12.21 ±0.81	8.57 ±0.53	14.10 ±0.34
B9	1.210 ±0.790	4.91 ±0.87	11.77 ±0.80	8.70 ±0.59	13.51 ±0.35
B10	3.18 ±0.80	4.27 ±0.80	12.22 ±0.66	8.89 ±0.40	13.98 ±0.29
w. Average	2.59 ±0.29	5.33 ±0.28	11.92 ±0.23	8.47 ±0.18	13.67 ±0.12
χ_R^2	1.29	1.14	1.09	0.94	0.63

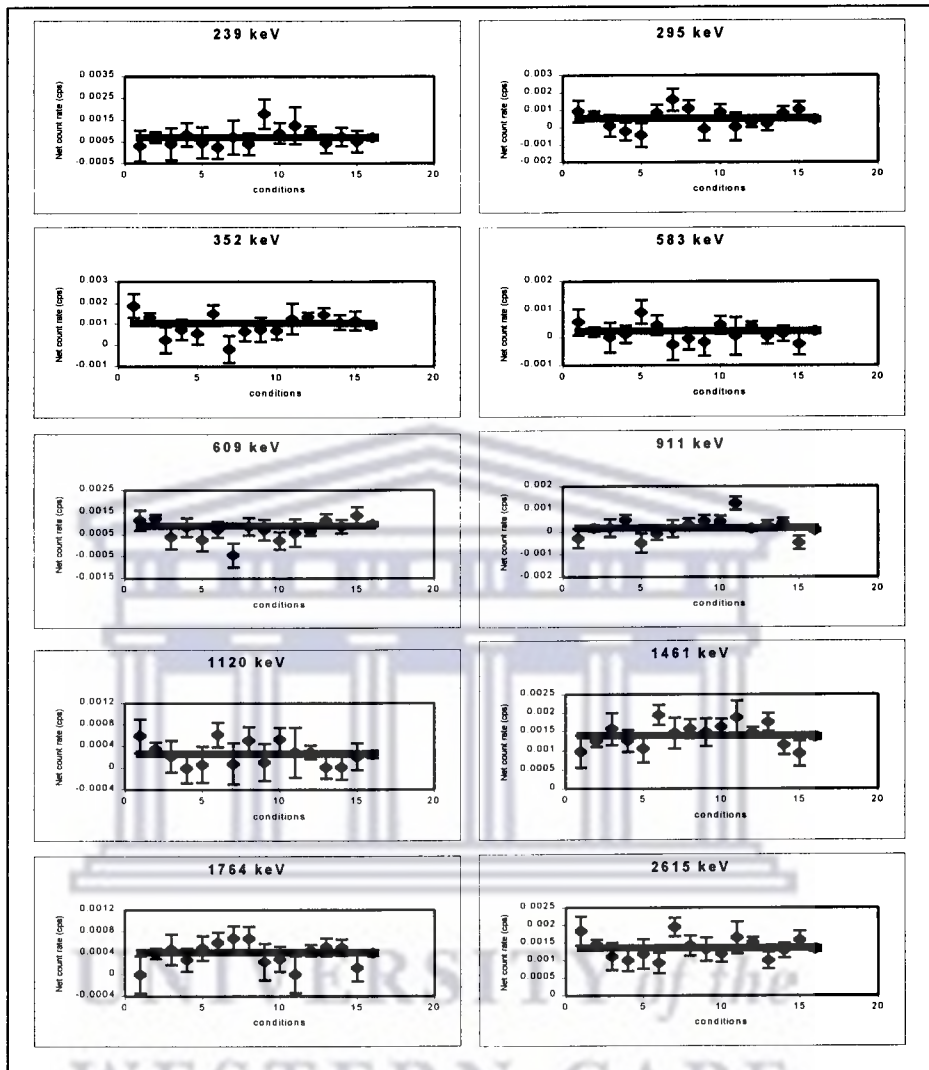


Figure A-2: This figure represents net count rates for background spectra acquired at different conditions (see Table A-3 to A-4) in the GMX detector system. The dark horizontal solid line represents the best fit through the weighted average value for the given energy. In this plots no significant difference can be observed in each energy plot, since most points lie within the statistical uncertainties. Radon circulation in the environment can affect the uranium series count rate, yet this plot does not show any major concern.

TABLE A-6: Background net count rate (10^{-3} cps) in the thorium and ^{40}K series of the HPGe detector system.

Energy→	239	583	911	2615	1461
Conditions↓	(keV)	(keV)	(keV)	(keV)	(keV)
B0	7.47 ± 1.39	10.14 ± 0.86	14.78 ± 0.80	39.6 ± 0.5	131.4 ± 0.9
B1	5.25 ± 0.87	9.54 ± 0.84	15.59 ± 0.90	40.0 ± 0.5	133 ± 1
B2	6.99 ± 1.26	10.16 ± 0.83	14.97 ± 0.82	39.7 ± 0.4	130.2 ± 0.9
B3	5.42 ± 0.82	7.90 ± 0.95	14.18 ± 0.62	39.9 ± 0.4	127.7 ± 0.8
B4	5.75 ± 1.15	9.37 ± 0.72	13.25 ± 0.78	39.5 ± 0.5	131 ± 1
B5	8.52 ± 1.24	8.92 ± 0.90	14.52 ± 0.58	40.1 ± 0.4	131.7 ± 0.7
B6	7.40 ± 1.61	8.22 ± 0.70	17.14 ± 0.93	40.2 ± 0.5	131 ± 1
B7	6.14 ± 0.92	8.33 ± 0.73	14.70 ± 0.47	40.0 ± 0.3	130.6 ± 0.7
B8	5.60 ± 0.85	9.61 ± 0.82	14.09 ± 0.76	40.1 ± 0.3	131.6 ± 0.7
B9	4.56 ± 1.00	9.31 ± 0.82	15.94 ± 0.65	40.4 ± 0.4	130.8 ± 0.7
B10	7.51 ± 0.83	9.53 ± 0.71	15.09 ± 0.46	39.8 ± 0.3	130.4 ± 0.6
w. Average	6.18 ± 0.35	9.17 ± 0.24	14.85 ± 0.25	39.9 ± 0.1	130.7 ± 0.4
χ_R^2	1.32	0.85	1.67	0.42	2.3

UNIVERSITY of the
WESTERN CAPE

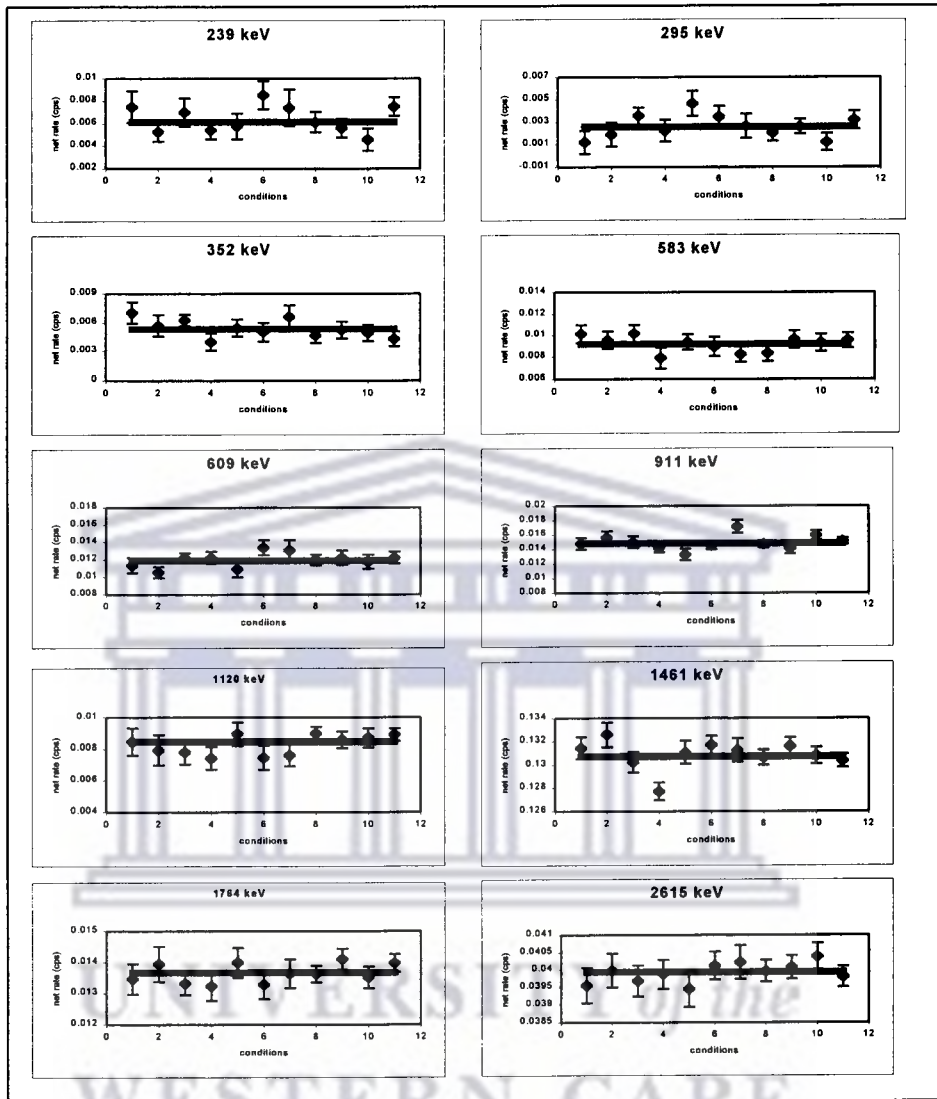


Figure A-3: This figure represents net count rates for background spectra acquired at different conditions (see Table A-5 to A-6) in the HPGe detector system. The dark horizontal solid line represents the best fit through the weighted average value for the given energy. In this plots no significant difference can be observed in each energy plot, since most points lie within the statistical uncertainties. Radon circulation in the environment can affect the uranium series count rate, yet this plot does not show any major concern.

Appendix B

Samples from a heavy mineral site.

TABLE B-1: Sample codes and their properties of origin. Included is also their sample mass and the spectra live times.

Sample code	Material type locations	Mass (kg)	Live time (s)
RME-S-4	Run-of mine, east trommel feed	0.2842	85793.87
RM-H-6	Run-of mine	0.3279	85763.89
RM-M-7	Run-of mine	0.3256	59633.81
RM-PA-1	Run-of mine	0.3240	8221.46
RM-T-2	Run-of mine	0.2897	10626.90
RMW-EB-3	Run-of mine, western trommel feed	0.3458	85788.58
RMW-S-4	Run-of mine, western trommel feed	0.2816	8161.61
WG-EB-3	Wet gravity feed	0.4633	85254.60
WG-ET-2	Wet gravity feed	0.3613	85725.52
WG-H-6	Wet gravity feed	0.5356	84845.16
WG-M-7	Wet gravity feed	0.5045	84947.73
WG-PA-1	Wet gravity feed	0.4069	85275.45
WG-S-4	Wet gravity feed	0.4135	85542.35

TABLE B-2: Sample codes and their properties of origin. Included is also their sample mass and the spectra live times.

Sample code	Material type locations	Mass (kg)	Live time (s)
ICP-PA-1	Ilmenite concentrate, attrition feed	0.5540	85759.49
MCA-EB-3	Magnetic concentrate, attrition feed	0.5299	57681.52
MCA-ET-2	Magnetic concentrate, attrition feed	0.4969	85784.04
MCA-H-6	Magnetic concentrate, attrition feed	0.5433	85740.17
MCA-M-7	Magnetic concentrate, attrition feed	0.4983	85751.17
MCA-PA-1	Magnetic concentrate, attrition feed	0.5425	8462.65
MCA-S-4	Magnetic concentrate, attrition feed	0.4822	8026.03
MC-ET-2	Magnetic concentrate	0.5216	82240.58
MC-S-4	Magnetic concentrate	0.5089	10178.06
NM-EB-3	Non-magnetic feed	0.4484	85261.43
NM-EF-2	Non-magnetic feed	0.4074	85463.47
NM-ET-3	Non-magnetic feed	0.4319	85265.68
NM-H-6	Non-magnetic feed	0.5309	84979.71
NM-M-7	Non-magnetic feed	0.4454	85034.48
NM-PA-1	Non-magnetic feed	0.5048	84931.10
NM-S-4	Non-magnetic feed	0.4179	85487.50
NS-1		0.7192	84492.29
NS-2		0.7164	84527.05
NS-3		0.7057	84514.43
NS-4		0.6964	84556.74
NSP-1		0.5422	8303.11
NSP-2		0.5383	8406.78
NSP-3		0.5200	8918.63

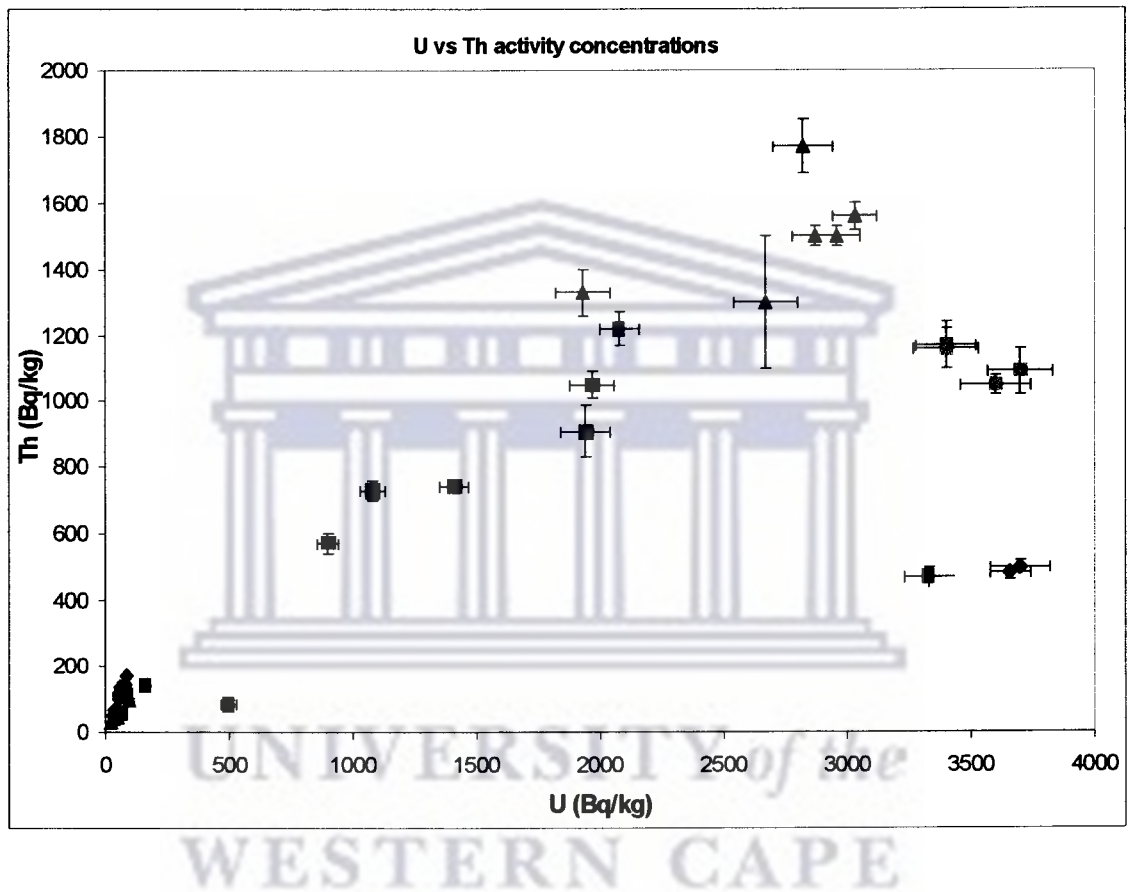


Figure B-1: The activity concentrations of uranium and thorium for all samples, relative to the activity concentration of ^{40}K as shown in Fig. 4-6 for all sampling locations.

Bibliography

- [Bro96] Browne E. and Firestone R.B. *Table of Radioactive Isotopes* (Ed. Shirley V.S.). John Wiley & Sons, New York (1996).
- [Chi00] Chiozzi P., de Felice P., Fazio A., Pasquale V., Verdoya M. *Laboratory application of NaI(Tl) γ -ray spectrometry to studies of natural radioactivity in geophysics*. Int. J. Appl. Radiat. Isot. **53**, 127 (2000).
- [Cro99] Croft S., Hutchinson I.G. *The measurement of U, Th and K concentrations in building materials*. Int. J. Appl. Radiat. Isot. **51**, 483 (1999).
- [Deb88] Debertain K., Helmer R.G. *Gamma- and X-ray spectrometry with semiconductor detectors*. Elsevier Science Publishers B.V., Amsterdam. (1988).
- [Deb89] Debertain K., Jianping R. *Measurement of the activity of radioactive samples in Marinelli beakers*. Nucl. Instr. Meth. **A278**, 541 (1989).
- [Dem97] De Meijer R.J., Stapel C., Jones D.G., Roberts P.D., Rozendaal A., Macdonald W.G., *Improved and new uses of radioactivity in mineral exploration and processing*, Exploration Mining Geology **6**, 105 (1997).
- [Dem98] De Meijer R.J., *Heavy minerals: from 'Edelstein' to Einstein*. J. Geochemical Exploration **62**, 81 (1998).
- [Dem01] De Meijer R.J., NAC, Faure, South Africa (2001) (*private communication*).
- [Dry89] Dryak P., Kovar P., Plchova L., Suran J., *Corrections for Marinelli geometry*, J. Radioanal. Nucl. Chem. **135**, 281 (1989).

- [Fel92] Felsmann M., Denk H.J., *Efficiency calibration of germanium detectors with internal standard*. J. Radioanal. Nucl. Chem. **157**, 47 (1992).
- [Gil95] Gilmore G., Hemingway J.D. *Practical gamma-ray spectrometry*. John Wiley & Sons, New York. (1995).
- [Jac87] Jackel B., Westmeier W., Patzelt P., *On the photopeak efficiency of germanium gamma-ray detectors*, Nucl. Instr. Meth. **A261**, 543 (1987).
- [Kno89] Knoll G. F. In *Radiation detection and measurement*. John Wiley & Sons, New York (1989).
- [Kra88] Krane K. In *Introductory Nuclear Physics*. John Wiley & Sons, New York (1988).
- [Lav97] Lavi N., Alfassi Z.B., Drndarski N., *Calibration of Marinelli vessels for measurement of radioactive environmental samples*, Nucl. Instr. Meth. **A385**, 376 (1997).
- [Leo87] Leo W.R., *Techniques for nuclear and particle physics experiments*, Springer-Verlag: Berlin, (1987).
- [Mal01] Maleka P.P., *Efficiency calibration (nuclide-specific) for the GMX gamma detector system at KVI*, Z114 KVI internal report, (2001).
- [Man88] Mann W.B., Rytz A., Spornol A., *Radioactivity measurement: principles and practice*, Int. J. Appl. Radiat. Isot. **39**, 717 (1988).
- [Nir98] Nir-El Y., *Application of reference materials in the accurate calibration of the detection efficiency of a low-level gamma-ray spectrometry assembly for environmental samples*, J. Radioanal. Nucl. Chem. **227**, 67 (1998).
- [Nun96] Nunez-Lagos R., Vitro A., *Shielding and background reduction*. Int. J. Appl. Radiat. Isot. **47**, 1011 (1996).
- [Par95] Park T.S., Jeon W.J., *Measurement of radioactive samples in Marinelli beakers by gamma-ray spectrometry*. J. Radioanal. Nucl. Chem. **193**, 133 (1995).
- [Tas96] Taskaeva M., Taskaev E., Penev I., *On the preparation of efficiency calibration standard for gamma-ray spectrometers*. Int. J. Appl. Radiat. Isot. **47**, 981 (1996).

- [Tro95] Tros G.H.J., de Meijer R.J., *A parameterisation of the HPGe detector γ -ray efficiency for a Marinelli beaker geometry (model 233N)*. A21 KVI internal report, (1995).
- [Van00] Van der Graaf E.R., Venema L.B., ten Have R., *NGD-KVI participation in the inter-laboratory test programme of NEN5697 'Radioactivity measurement: Determination of natural radioactivity in dense building materials by means of semiconductor gamma-ray spectrometry'*, S64 KVI internal report, (2000).
- [Ven00] Venema L.B., de Meijer R.J., *Natural radionuclide as tracers of the dispersal of dredge spoil dumped at sea*, J. Environmental radioactivity, (accepted in 23 october 2000).
- [Ver92] Verplancke J., *Low level gamma spectroscopy: low, lower, lowest*, Nucl. Instr. Meth. **A312**, 174 (1992).



UNIVERSITY *of the*
WESTERN CAPE